JACS
JOURNAL OF THE AMERICAN CHEMICAL SOCIETY
Article
pubs.acs.org/JACS

Unravelling the Structure of Magnus' Pink Salt

Bryan E. G. Lucier,[†] Karen E. Johnston,[†] Wenqian Xu,[‡] Jonathan C. Hanson,[‡] Sanjaya D. Senanayake,[‡] Siyu Yao,[§] Megan W. Bourassa,[∥] Monika Srebro,[⊥,#] Jochen Autschbach,*[,⊥] and Robert W. Schurko*[,†]

[†]Department of Chemistry and Biochemistry, University of Windsor, Windsor, Ontario, Canada N9B 3P4
[‡]Department of Chemistry, Brookhaven National Laboratory, Upton, New York 11973, United States
[§]Center for Computational Science & Engineering, and PKU Green Chemistry Centre, Peking University, Beijing 100871, China
[∥]Department of Chemistry, Stony Brook University, Stony Brook, New York 11794, United States
[⊥]Department of Chemistry, University at Buffalo, State University of New York, Buffalo, New York 14260-3000, United States
[#]Department of Theoretical Chemistry, Faculty of Chemistry, Jagiellonian University, 30-060 Krakow, Poland

Supporting Information

ABSTRACT: A combination of multinuclear ultra-wideline solid-state NMR, powder X-ray diffraction (pXRD), X-ray absorption fine structure experiments, and first principles calculations of platinum magnetic shielding tensors has been employed to reveal the previously unknown crystal structure of Magnus' pink salt (MPS), $[Pt(NH_3)_4][PtCl_4]$, study the isomeric Magnus' green salt (MGS), $[Pt(NH_3)_4][PtCl_4]$, and examine their synthetic precursors K_2PtCl_4 and $Pt(NH_3)_4Cl_2 \cdot H_2O$. A simple synthesis of MPS is detailed which produces relatively pure product in good yield. Broad ^{195}Pt, ^{14}N, and ^{35}Cl SSNMR powder patterns have been acquired using the WURST-CPMG and BRAIN-CP/WURST-CPMG pulse sequences. Experimentally measured and theoretically calculated platinum magnetic shielding tensors are shown to be very sensitive to the types and arrangements of coordinating ligands as well as intermolecular Pt−Pt metallophilic interactions. High-resolution ^{195}Pt NMR spectra of select regions of the broad ^{195}Pt powder patterns, in conjunction with an array of ^{14}N and ^{35}Cl spectra, reveal clear structural differences between all compounds. Rietveld refinements of synchrotron pXRD patterns, guided by first principles geometry optimization calculations, yield the space group, unit cell parameters, and atomic positions of MPS. The crystal structure has *P*-1 symmetry and resides in a pseudotetragonal unit cell with a distance of >5.5 Å between Pt sites in the square-planar Pt units. The long Pt−Pt distances and nonparallel orientation of Pt square planes prohibit metallophilic interactions within MPS. The combination of ultra-wideline NMR, pXRD, and computational methods offers much promise for future investigation and characterization of Pt-containing systems.

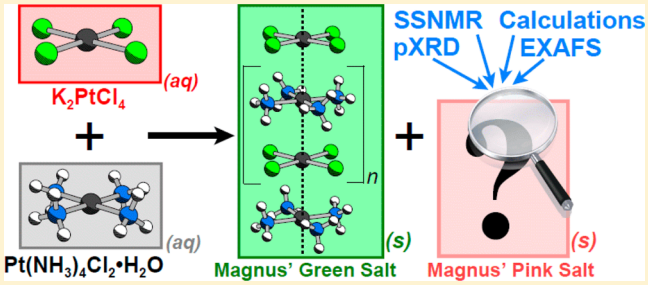

INTRODUCTION

The most commonly encountered structural motif for platinum in the 2+ oxidation state is the square-planar complex. Square-planar Pt(II) complexes are of great interest, both in terms of their synthesis and usage in many areas of chemistry[1−8] and biology.[8−16] Much research has been devoted toward the development of optically active materials with "tunable" absorption and/or emission wavelengths, with practical applications in devices such as solid-state sensors, electronic switches, or laser-based devices. In particular, systems that are based on a central square-planar Pt(II) motif often exhibit unique optical properties, which are attributed to the metal−ligand interactions, Pt−Pt metallophilic interactions between adjacent layers, or both.[5,17−21] The strength of the metallophilic interaction[22−25] and concomitant optical/electronic activity often rely strongly on the Pt−Pt distance.

Two classic examples of colorful Pt complexes featuring metallophilic interactions are Magnus' salts, which have a long history of eluding structural characterization. Magnus' green salt (MGS), $[Pt(NH_3)_4][PtCl_4]$, is a highly insoluble "double-salt" initially reported by Magnus in 1828[26] and characterized as a one-dimensional polymeric complex of square-planar Pt layers (Scheme 1) over 100 years later in 1957.[27] The green color of MGS is attributed to nearest-neighbor Pt−Pt metallophilic interactions between adjacent layers.[28,29] For derivatives of MGS, a variety of colors, depending on temperature and coordinating ligands, is often observed and thought to be the result of modification of the Pt−Pt distance between square-planar layers.[18,30,31] Interestingly, an elusive product known as Magnus' pink salt (MPS) may result during the synthesis of MGS under certain reaction conditions, although the isolation of a pure MPS product (without a MGS coproduct) is very challenging.[27,30,32,33] It is postulated

Received: July 24, 2013
Published: December 13, 2013

   dx.doi.org/10.1021/ja4076277 | *J. Am. Chem. Soc.* 2014, 136, 1333−1351

Scheme 1. Schematic Representations of (a) K_2PtCl_4, (b) $Pt(NH_3)_4Cl_2{\cdot}H_2O$, (c) MGS ($[Pt(NH_3)_4][PtCl_4]$), and (d) MPS ($[Pt(NH_3)_4][PtCl_4]$)[a]

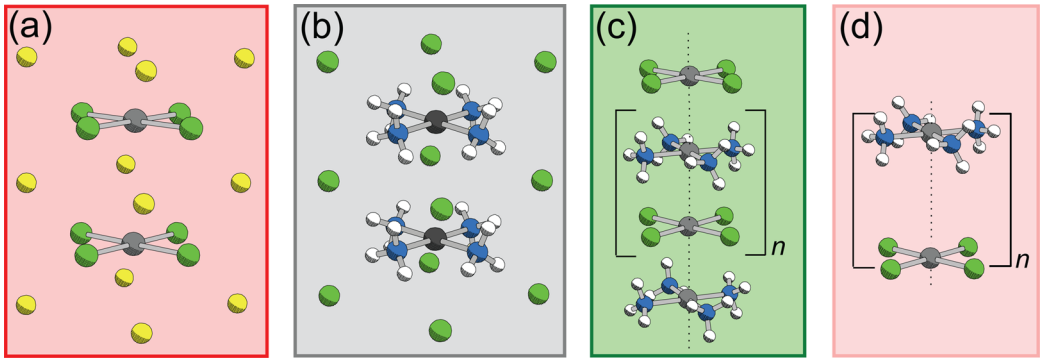

[a]Depictions are based on experimentally determined crystal structures, except for MPS, which previously has been postulated to adopt the shown arrangement but has no reported crystal structure to date. Water molecules in (b) are omitted for clarity.

that MPS exhibits only a faint pink color due to a longer Pt−Pt distance than that of MGS and corresponding reduction in the strength of the Pt−Pt metallophilic interaction. Since MPS rapidly converts to MGS in solution, the growth of pure MPS crystals suitable for conclusive single-crystal X-ray diffraction (XRD) studies has proved elusive to date. The structure and composition of MPS are believed to be otherwise identical to MGS.[27]

Structural characterization of such systems is challenging, particularly when XRD studies provide limited or no information (e.g., in cases of amorphous or partially disordered solids, or incident X-ray beam absorption by the compound, which sometimes arises in the study of Pt-based materials). The nature of the coordinating platinum environment determines the reactivity and stability of the complex; however, it is often difficult to probe this structural environment using conventional methods. Platinum-containing compounds are often characterized using optical spectroscopy, solution-state NMR (^{1}H, ^{13}C, and ^{195}Pt) and X-ray crystallography. In the case of highly soluble complexes, ^{195}Pt solution-state NMR is a useful and widely employed characterization method,[34−38] while limited additional information is available from ^{1}H and ^{13}C solution NMR of organic ligands. Of course, ^{195}Pt solution NMR does not provide any information on long-range order, metallophilic interactions, accurate measures of platinum chemical shift anisotropy (CSA), etc. due to the dissociation of solid complexes in solution into constituent ions. Many platinum-based compounds have low solubilities, which restricts or altogether prohibits the use of solution-state NMR. Structural determination using XRD techniques is limited by (i) the ability to produce suitable single crystals and (ii) the crystallinity of the sample. In many cases, solid-state NMR (SSNMR) is ideal for structural characterization, as a complementary or standalone technique. In particular, SSNMR experiments on NMR-active transition-metal nuclei, such as ^{195}Pt, can act as powerful structural probes for a wide array of materials.

The platinum NMR chemical shift (CS) is extremely sensitive to the local platinum environment and has a known range of ca. 15 000 ppm.[39,40] ^{195}Pt SSNMR powder patterns of square-planar platinum compounds yield information on the anisotropic chemical shift tensor and local electronic structure; however, they are often very broad and require time-consuming experiments to acquire. Conventional static and magic-angle spinning (MAS) ^{195}Pt NMR experiments often result in low signal-to-noise (S/N) ratios and spectra of poor quality. Experiments involving direct excitation (DE) of ^{195}Pt are often very lengthy, as ^{195}Pt T_1 values are usually on the order of tens of seconds to minutes in length. Cross-polarization (CP) experiments are an option but are often ineffective. Under static conditions, the excitation bandwidths are extremely limited, and under the fast MAS conditions that are required for broad patterns, CP efficiency is greatly reduced. Furthermore, MAS experiments require that the magic angle be tuned with very high precision; even with accurate tuning, the low S/N and non-uniform distribution of signal over the manifold of spinning sidebands often yields unreliable CS tensor parameters.[41]

Recently, our research group introduced two pulse sequences that are effective for the efficient acquisition of ultra-wideline (UW) powder patterns. The wideband uniform-rate smooth-truncation Carr−Purcell Meiboom−Gill (WURST-CPMG) pulse sequence[42−46] is an echo-type sequence which employs WURST-80 pulses[45] for broadband excitation and a CPMG echo train for T_2-dependent accumulation of echoes.[47] As an alternative to DE, if broadband CP is required, the broadband adiabatic inversion pulses for cross-polarization (BRAIN-CP) pulse sequence may be applied.[48] BRAIN-CP features a rectangular pulse on the H-channel and a WURST-80 pulse on the X-channel, which serve to transfer polarization and store it along the $-z$-axis. A broadband conversion pulse is used to rotate polarization into the transverse plane. BRAIN-CP is easily combined with WURST-CPMG (the combination of the two has been termed BRAIN-CP/WURST-CPMG). For brevity, WURST-CPMG and BRAIN-CP/WURST-CPMG experiments are referred to as DE and CP experiments, respectively. Both sequences are very useful for acquiring ^{195}Pt NMR spectra and render many previously uninvestigated platinum-containing compounds as plausible targets for ^{195}Pt SSNMR characterization.[41,49,50]

Herein, the use of multinuclear SSNMR experiments to study Magnus' salts and their associated starting reagents is discussed. ^{195}Pt SSNMR experiments conducted using the WURST-CPMG, BRAIN-CP/WURST-CPMG, and conventional Hahn-echo pulse sequences reveal spectra which can be correlated to subtle structural differences between the two systems, via extraction of the platinum CS tensor parameters. ^{14}N and ^{35}Cl ultrawideline SSNMR experiments are also utilized to probe the molecular structures and assess sample

dx.doi.org/10.1021/ja4076277 | J. Am. Chem. Soc. 2014, 136, 1333−1351

purity. Powder XRD experiments and concomitant Rietveld refinements guided by density functional theory (DFT) calculations are utilized to comprehensively characterize the structure of MPS. DFT calculations of platinum nuclear magnetic shielding (MS) tensors, as well as an analysis of localized molecular orbitals which most influence shielding, lend insight into the relationships between NMR parameters and molecular structure. X-ray absorption fine structure (EXAFS) data provide information on Pt-ligand binding and bond distance in MPS. Finally, we propose a comprehensive structural model of MPS based on SSNMR, pXRD, and EXAFS data. The elegant blend of pXRD, SSNMR, and computational methods[49,51−64] allows for significant insight into Magnus' salts and their precursors, and our model of MPS demonstrates the possible applications of these combined methodologies for the study of a wide array of Pt-containing systems.

EXPERIMENTAL SECTION

Sample Identities. $Pt(NH_3)_4Cl_2{\cdot}H_2O$ [tetraamine platinum(II) chloride monohydrate], K_2PtCl_4 [potassium tetrachloroplatinate(II)], and $[Pt(NH_3)_4][PtCl_4]$ (MGS) [tetraamine platinum(II) tetrachloroplatinate(II)] were purchased from Strem Chemicals, Inc. and used without further purification.

Synthesis of MPS. Syntheses of MPS were attempted utilizing previously reported procedures;[18,27,30,65−67] however, we were unable to attain a reasonably pure, stable sample of MPS using these routes. Hence, a synthetic procedure was designed and optimized, which is detailed as follows: two individual 0.0026 M reagent solutions were prepared in separate flasks by dissolving either $Pt(NH_3)_4Cl_2{\cdot}H_2O$ (30 mg) or K_2PtCl_4 (37 mg) in 3 mL H_2O, followed by the addition of 31 mL acetone while stirring. All solutions and glassware were cooled to near 0 °C. Although acetone and water are generally miscible, the disparate volumes of water and acetone, low temperature of the system, and visual evidence of turbidity suggest that some degree of phase separation or containment (i.e., reverse micelles) was present. The individual reagent solutions were then stirred and subsequently combined. The resulting solution was stirred momentarily and then allowed to stand unagitated for ca. 10 s while a pink precipitate formed. The product was obtained as a pink powder via vacuum filtration of the reaction solution on a prechilled fine glass frit. The product was first washed with chilled acetone to remove any water from the sample via displacement and minimize MGS coproduct formation. Following this, the product was washed with a minimal amount (<10 mL) of chilled water to remove residual water-soluble reagents, $Pt(NH_3)_4Cl_2{\cdot}H_2O$ and K_2PtCl_4, followed by a final wash with chilled acetone. Once dry, the frit and product were heated at 120 °C for at least 2 h in a lab oven to remove any trace acetone and water. The product was removed from the frit, and its identity and purity were confirmed in a preliminary manner via known absorptions in its IR spectrum[30] (Table S1, Figure S1) as well as elemental analysis (Table S2) and ^{1}H SSNMR (Table S3, Figure S2). The isolated yield of MPS was 70%.

It is noted that after formation as a precipitate in solution, MPS rapidly converts to MGS if it is not removed from solution and dried. It takes ca. 6−12 h for this conversion to occur to completion in the acetone/water volumes used in this synthesis. This transformation occurs much more rapidly at higher H_2O concentrations, particularly as the product dries on the frit. In addition, if the frit is moist when heated afterward, any MPS powder located on damp regions rapidly converts to MGS. Once isolated after heating, MPS is stable for at least 6 months (confirmed via SSNMR and IR analyses) under normal atmospheric conditions but rapidly converts to MGS if exposed to bulk water or aqueous solution.

Solid-State NMR. All ^{1}H, ^{195}Pt, and ^{14}N solid-state NMR spectra were collected on a Varian Infinity Plus NMR spectrometer with an Oxford 9.4 T wide-bore magnet with $\nu_0(^1H)$ = 399.73 MHz, $\nu_0(^{195}Pt)$ = 85.59 MHz, and $\nu_0(^{14}N)$ = 28.89 MHz. All ^{1}H, ^{195}Pt, and ^{14}N static (i.e., stationary sample) NMR experiments were conducted using a Varian/Chemagnetics 5 mm HX static probe. ^{195}Pt and ^{1}H MAS experiments were performed using a Varian/Chemagnetics 2.5 mm HX probe. All samples for static experiments were packed into 5 mm o.d. zirconia rotors or glass tubes, and samples for MAS experiments were packed into 2.5 mm o.d. zirconia rotors. A Chemagnetics low-γ tuning accessory and preamplifier were used on the X channel for all ^{14}N NMR experiments. Platinum chemical shifts were referenced with respect to 1.0 M Na_2PtCl_6 (aq) (δ_{iso} = 0.0 ppm), and nitrogen chemical shifts were reported with respect to NH_4Cl (s) (δ_{iso} = 0.0 ppm). All ultrahigh field ^{35}Cl static NMR experiments were performed on a 21.1 T Bruker Avance II NMR spectrometer ($\nu_0(^{35}Cl)$ = 88.13 MHz) at the National Ultrahigh-field NMR Facility for Solids in Ottawa, Ontario, Canada. Spectra were acquired on a home-built 4 mm HX probe, with samples packed into 4 mm o.d. glass NMR tubes. Chlorine chemical shifts were referenced to NaCl (s) (δ_{iso} = 0.0 ppm). Continuous-wave ^{1}H decoupling was employed for all ^{195}Pt, ^{14}N, and ^{35}Cl experiments. Detailed lists of parameters for all of the experiments discussed below are summarized in Tables S4−S12.

^{195}Pt, ^{14}N, and ^{35}Cl static UW NMR experiments were conducted using the WURST-CPMG pulse sequence.[42−46] Since powder patterns are too broad to acquire in a single experiment, frequency-stepped acquisitions of individual subspectra were required, with the overall powder patterns constructed from the coaddition or skyline projection of subspectra.[68−71] ^{195}Pt and ^{14}N NMR experiments used a 50 μs WURST-80 pulse, a sweep rate of 40 MHz/ms from high to low frequency over 2000 kHz, and a spectral width of 2000 kHz. ^{195}Pt and ^{14}N WURST-CPMG experiments used 200 and 110 points per echo, respectively, with experimentally optimized rf powers of 44 and 30 kHz, respectively, and proton decoupling fields ranging from 24 to 37 kHz. For all ^{35}Cl WURST-CPMG NMR experiments, a spectral width of 1000 kHz and WURST sweep rate of 20 MHz/ms from high to low frequency were used, along with a ^{35}Cl rf power of 35 kHz and ^{1}H decoupling power of 20 kHz.

^{1}H−^{14}N BRAIN-CP/WURST-CPMG experiments[48] employed a Hartmann−Hahn matching field of 22 kHz, CP sweep rate of 40 kHz/ms across a total range of 400 kHz, refocusing WURST pulses across a range of 450 kHz, ^{1}H $\pi/2$ pulse widths of 4.00 μs, spectral widths of 2000 kHz, and ^{1}H decoupling fields of 25 kHz. The complete ^{14}N WURST-CPMG and BRAIN-CP/WURST-CPMG NMR spectra were generated by mirroring the low-frequency (right) portion of the powder pattern about δ = 0 ppm, as described previously.[41,72]

Static ^{195}Pt NMR spectra of discontinuity regions (vide infra) were acquired using a standard Hahn-echo experiment of the form $(\pi/2)_x - \tau_1 - (\pi)_y - \tau_2 -$ acq, where τ_1 and τ_2 represent interpulse delays of 40 and 20 μs, respectively. A $\pi/2$ pulse width of 2.50 μs and spectral width of 2000 kHz were used, except for the low-frequency Hahn-echo experiment for MGS, where a $\pi/2$ pulse width of 6.63 μs and spectral width of 200 kHz were used. Corresponding ^{1}H−^{195}Pt static CP Hahn-echo NMR experiments employed ^{1}H $\pi/2$ pulse widths of 3.93 μs, a spectral width of 500 kHz, a Hartmann−Hahn matching field of 29 kHz, and a ^{1}H decoupling field of 37 kHz. ^{1}H−^{195}Pt BRAIN-CP/WURST-CPMG experiments[48] used a Hartmann−Hahn matching field of 29 kHz and CP sweep rate of 100 kHz/1 ms across a total range of 500 kHz, resulting in a total contact time of 5 ms. The total contact time of a BRAIN-CP/WURST-CPMG experiment is determined by the ratio of the sweep range to the sweep rate. ^{1}H−^{195}Pt BRAIN-CP/WURST-CPMG experiments also used refocusing WURST pulses across a range of 2000 kHz, ^{1}H $\pi/2$ pulse widths of 3.93 μs, spectral widths of 2000 kHz, and a ^{1}H decoupling field of 24 kHz. ^{195}Pt MAS NMR spectra of MGS were acquired using a standard Bloch-decay experiment, with a $\pi/2$ pulse width of 1.13 μs and spectral width of 1500 kHz. ^{1}H decoupling fields in excess of 70 kHz were applied for all MAS experiments.

^{1}H MAS NMR spectra were acquired at a spinning speed of 25 kHz using a standard Bloch decay pulse sequence, with a $\pi/2$ pulse width of 3.0 μs, spectral width of 200 kHz, and recycle delay of 2 s.

Simulations of all static solid-state NMR spectra were performed using the WSOLIDS software package.[73] In all cases, uncertainties in extracted NMR tensor parameters for static spectra were estimated by

dx.doi.org/10.1021/ja4076277 | J. Am. Chem. Soc. 2014, 136, 1333−1351

visual inspection of best fit spectra and bidirectional variation in simulation parameters. Simulations of ^{195}Pt MAS NMR spectra were performed using the DMFit software program.[74]

Theoretical Calculations. DFT computations of the platinum nuclear MS tensors were performed with a developer's version of the Amsterdam Density Functional (ADF) package[75,76] using the hybrid variant of the Perdew−Burke−Ernzerhof (PBE) functional,[77,78] PBE0.[79,80] A relativistic all-electron triple-ζ singly polarized (TZP) basis set from the ADF basis set library was employed for all atoms, except Pt for which the more flexible quadruple-ζ quadruply polarized (QZ4P) basis was used. As previous studies have shown, this basis set combination is well suited for efficient and reasonably accurate computations of Pt magnetic shielding tensors.[36,81−83] Relativistic effects were incorporated in the computations by means of the zeroth-order regular approximation (ZORA).[84−86] In the numerical integration method used for the calculations, the general accuracy parameter was set to 4.0, while for the atomic core regions the accuracy parameter was set to 5.0. A criterion of 10^{-4} au was applied to remove linearly dependent basis function combinations. Natural bond orbital (NBO) and natural localized molecular orbital (NLMO) analyses were applied for the MS tensors.[87,88] Details of the technique and a brief description of the sequence of calculations are discussed elsewhere.[82,89] To ensure that all basis set functions were used in the analysis, the linear dependency criterion was decreased to 10^{-5} au. Symmetry was not explicitly utilized in the calculations.

In the case of MGS, $Pt(NH_3)_4Cl_2{\cdot}H_2O$ and K_2PtCl_4 systems, MS parameters were calculated from model clusters extracted from experimental and/or optimized solid-state geometries (vide infra) in such a way to ensure the surroundings of the central Pt unit(s) were as close to the crystal environment as possible. Geometry optimizations of the atomic positions were performed with periodic boundary conditions, using experimental lattice constants.[27,90,91] The optimizations utilized the Plane-Wave Self-Consistent Field (PWscf) package,[92] version 4.2.1 and 5.0.2 from the Quantum-ESPRESSO suite of programs.[93] In the PWscf calculations the PBE functional was employed in conjunction with ultrasoft pseudopotentials (USPPs)[94] and plane-wave (PW) basis sets for the valence orbitals. The core levels and radii (in au) were [He](1.3), [He](1.4), [Ne](1.5), [Ar](1.6), and [Xe + 4f](1.8) for N, O, Cl, K, and Pt, respectively. For H, an "all-electron pseudopotential" was generated with a core radius of 0.9 au. The kinetic energy cutoff for the PW basis sets was set to 40 Ry. A *k*-point sampling of 3 × 3 × 5 for MGS and 4 × 4 × 7 for reagents was used. The geometry optimizations were successful in closely reproducing the experimental geometric parameters for MGS and K_2PtCl_4. In the case of $Pt(NH_3)_4Cl_2{\cdot}H_2O$, the calculated Pt−N distances are much smaller than those determined from an X-ray crystal structure.[90] The latter, more than 2.6 Å, seem to be unreasonably large, given typical Pt−N distances in square-planar Pt moieties such as Benton's salt, $Pt(NH_3)_4CuCl_4$, (2.04 Å)[95] or MGS (2.08 Å). We consider the calculated Pt−N distance of $Pt(NH_3)_4Cl_2{\cdot}H_2O$ more reliable than the experimental estimate (vide infra). In the case of MGS, stricter than default geometry convergence criteria were applied to match the experimental structure.

Analogous geometry optimizations of the atomic positions with periodic boundary conditions were also performed to refine the proposed MPS structural model. A *k*-point sampling of 5 × 5 × 4 was used in these calculations. For the calculated structure (Figure B13, Appendix B, Supporting Information), a molecular cluster approach was examined for the purpose of conducting calculations of NMR interaction tensors. However, all of our attempts to obtain an adequately converged ground state as well as platinum MS parameters failed for this system. These difficulties are not unexpected, since the DFT methodology has known problems with spatially separated subsystems, due to the tendency of approximate functionals to spread out charges and energetically to prefer a delocalized electron density over a localized density.[96] In the NMR calculations, there are likely to be spurious charge-transfer excitations[97] that (implicitly) contaminate the platinum magnetic shielding results for MPS. Although the large spatial separation of the complex ions renders DFT calculations of larger MPS clusters unreliable, it might allow, however, for an electrostatic treatment of the interactions in the solid. Consequently, MS parameters for particular platinum units in the MPS crystal structure were calculated using point-charge embedding. In specific, the chloride and ammonium Pt ions were placed in the center of a 7 × 7 × 7 supercell of point charges located at the atomic positions of the MPS crystal. The charges were taken to be the Mulliken charges, calculated for the MPS structure with the BAND program in the ADF package, using the TZP Slater-type basis sets. For the geometry-optimized atomic coordinates of MPS and their corresponding Mulliken charge values, please see Table S13.

Powder X-ray Diffraction and Rietveld Refinements. Room-temperature powder X-ray diffraction (pXRD) experiments were completed at beamline X7B at the National Synchrotron Light Source (NSLS) of Brookhaven National Lab (BNL). Powdered samples were loaded into 0.5 ID Kapton capillaries. A Perkin-Elmer amorphous silicon area detector was used to collect XRD images in transmission mode. Fit2D was used to integrate two-dimensional data to one dimension.[98] Rietveld refinements[99] and Lebail fittings were performed on MGS and MPS using the GSAS software.[100,101] The wavelength used was 0.3196 Å. The Rietveld refinements were performed using experimental pXRD data with a 2θ range from 1.5 to 22°. Soft restraints were applied to Pt−Cl and Pt−N bond distances. Pt−Cl bonds were constrained to 2.32 ± 0.10 Å, and Pt−N bonds were constrained to 2.05 ± 0.10 Å. An overall displacement parameter was refined for all atoms. The background was fitted with a Chebyschev function of 14 terms, and the peak profile was fitted with a pseudo-Voigt function.

X-ray Absorption Fine Structure. X-ray Absorption Near Edge Spectroscopy (XANES) and Extended X-ray Absorption Fine Structure (EXAFS) measurements of the Pt complexes were collected at beamline X19A of the NSLS at BNL using a Si (111) monochromator (2×10^{-4} ($\Delta E/E$)). All the measurements were collected under transmission mode with an optimized ion chamber at the Pt L_{III} edge (11564 eV). The Pt salts were diluted to 20% wt using fine BN powder and pressed to make 2 mm thick pellets for measurements. XANES and EXAFS spectra of the samples were analyzed using the Athena and Artemis programs employing the Feff 6.0 package.

Elemental Analysis. Microanalyses were performed on samples of MPS using a Perkin-Elmer 2400 Series II C, H, N analyzer in the Centre for Catalysis and Materials Research at the University of Windsor. Elemental analysis results are summarized in Table S2.

Infrared Spectroscopy. Fourier-transform infrared (FTIR) spectra were acquired using a Nicolet Magna 860 FTIR spectrometer coupled to a Continμum IR microscope (Thermo-Nicolet, Madison, WI) at beamline U2B in the NSLS. The microscope was equipped with a 32× Schwarzschild objective and a liquid nitrogen cooled mercury cadmium telluride detector. A thin layer of each sample was placed on a 1 mm thick calcium fluoride slide, and point spectra were acquired with a 50 μm aperture in transmission mode. For each spectrum, 64 scans were co-added with a 4 cm^{-1} spectral resolution over the mid-infrared region (1000−4000 cm^{-1}).

■ RESULTS AND DISCUSSION

To begin, NMR spectra acquired with the ^{195}Pt WURST-CPMG and ^{1}H−^{195}Pt BRAIN-CP/WURST-CPMG pulse sequences are presented and discussed. High-resolution ^{195}Pt Hahn-echo and ^{1}H−^{195}Pt CP-echo spectra of key diagnostic spectral regions are then presented, followed by ^{195}Pt MAS NMR spectra. ^{14}N WURST-CPMG and ^{1}H−^{14}N BRAIN-CP/WURST-CPMG experiments yield spectra which shed additional light on intermolecular interactions. Then, ^{35}Cl WURST-CPMG spectra of all systems are compared and contrasted and related to differences in structure and symmetry. A brief discussion of EXAFS and XANES experimental data is included. Powder XRD patterns and corresponding refinements, which were used to differentiate the compounds and conduct a structural analysis of MPS, are then discussed in

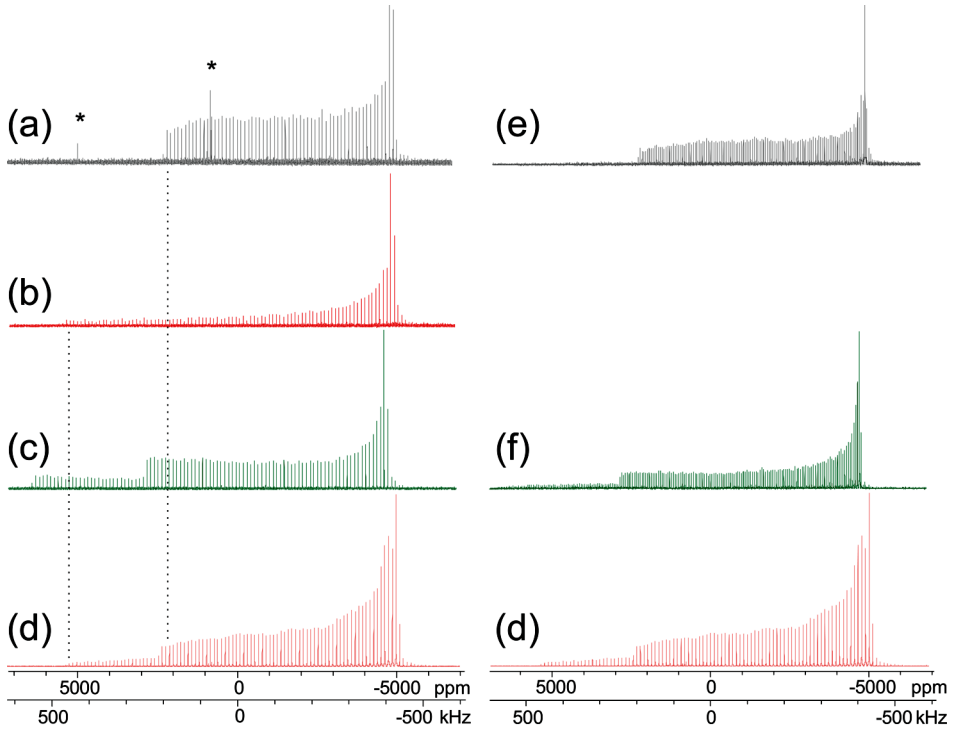

Figure 1. ^{195}Pt static WURST-CPMG NMR spectra of (a) $Pt(NH_3)_4Cl_2{\cdot}H_2O$, (b) K_2PtCl_4, (c) MGS, and ^{1}H−^{195}Pt static BRAIN-CP/WURST-CPMG NMR spectra of (d) MPS, (e) $Pt(NH_3)_4Cl_2{\cdot}H_2O$, and (f) MGS. Asterisks (*) denote interference from local FM radio stations. Dashed lines indicate the high-frequency edge (δ_{11}) of the powder patterns of the starting reagents. The (d) spectrum is shown at the bottom of each column for comparison to the spectra above (see text for details).

Table 1. Platinum Chemical Shift Tensor Parameters Determined from ^{195}Pt Static and MAS NMR Experiments[a]

compound	method[b]	δ_{11} (ppm)	δ_{22} (ppm)	δ_{33} (ppm)	δ_{iso} (ppm)[c]	Ω (ppm)[d]	κ[e]
K_2PtCl_4[50]	W	5437(90)	−4983(69)	−4983(69)	−1510(60)	10420(100)	−1.00[a]
$Pt(NH_3)_4Cl_2{\cdot}H_2O$	E	2248(41)	−4916(35)	−4952(29)	−2540(20)	7200(50)	−0.99(1)
	CE	2248(41)	−4916(35)	−4952(29)	−2540(20)	7200(50)	−0.99(1)
	W	2257(93)	−4884(84)	−4992(73)	−2540(60)	7250(100)	−0.97(2)
	M	2043(470)	−4607(314)	−4957(272)	−2507(10)	7000(700)	−0.90(10)
green salt $[PtCl_4]^{2-}$	E	6630(25)	−4770(40)	−4770(40)	−970(15)	11400(30)	−1.00(1)
	W	6563(90)	−4737(102)	−4737(102)	−970(60)	11300(100)	−1.00(2)
	BC	6563(52)	−4737(57)	−4737(57)	−970(40)	11300(50)	−1.00(1)
	M	–	–	–	−970(6)	–	–
green salt $[Pt(NH_3)_4]^{2+}$	E	2835(22)	−4725(27)	−4725(27)	−2205(10)	7560 (30)	−1.00(1)
	W	2795(90)	−4705(85)	−4705(85)	−2205(60)	7500(100)	−1.00(2)
	BC	2828(52)	−4722(50)	−4722(50)	−2205(40)	7550(50)	−1.00(1)
	M	–	–	–	−2208(6)	–	–
pink salt $[PtCl_4]^{2-}$	CE	5530(48)	−5045(49)	−5045(39)	−1520(30)	10575(50)	−1.00(1)
	BC	5473(91)	−4975(77)	−5028(71)	−1510(60)	10500(100)	−0.99(1)
pink salt $[Pt(NH_3)_4]^{2+}$	CE	2367(29)	5014(26)	−5033(23)	−2560(20)	7400(30)	−0.99(1)
	BC	2373(84)	−5027(65)	−5027(61)	−2560(50)	7400(100)	−1.00(1)
	M	–	–	–	−2560(6)	–	–

[a]The uncertainties in δ_{iso}, Ω, and κ were measured from experimental spectra and corresponding simulations. The uncertainties in individual CS tensor components (δ_{11}, δ_{22}, δ_{33}) were mathematically propagated from the formulas used to calculate δ_{iso}, Ω, and κ. The $[PtCl_4]^{2-}$ units in K_2PtCl_4 have local C_4 symmetries; thus, CS tensors must be of axial symmetry, and values of κ = 1.0. [b]E = Hahn echo experiment, W = WURST-CPMG experiment, M = MAS experiment, CE = ^{1}H−^{195}Pt cross-polarized Hahn echo experiment, BC = ^{1}H−^{195}Pt BRAIN-CP/WURST-CPMG experiment. [c]Isotropic chemical shift: $\delta_{iso} = (\delta_{11} + \delta_{22} + \delta_{33})/3$. [d]Span: $\Omega = \delta_{11} - \delta_{33}$. [e]Skew: $\kappa = 3(\delta_{22} - \delta_{iso})/\Omega$.

dx.doi.org/10.1021/ja4076277 | J. Am. Chem. Soc. 2014, 136, 1333−1351

detail. A proposed structural model of MPS is presented from a combination of SSNMR, XRD, and EXAFS data, along with geometry optimization calculations. Finally, first principles calculations of platinum nuclear magnetic shielding (NMR) tensors for several model systems are compared with the experimentally derived data and interpreted in terms of local bond and lone-pair contributions.

^{195}Pt WURST-CPMG Experiments. ^{195}Pt NMR spectra of $Pt(NH_3)_4Cl_2{\cdot}H_2O$, K_2PtCl_4, and MGS are shown in Figure 1a,b,c, with corresponding CS tensor parameters found in Table 1. The K_2PtCl_4 spectrum was previously discussed in a separate work.[50] The ^{195}Pt powder patterns are indicative of single platinum sites each possessing axially symmetric CS tensors with $\kappa \approx -1$ (i.e., δ_{11} is the distinct component and $\delta_{22} \approx \delta_{33}$); axially symmetric tensors of this sort are commonly observed in square-planar Pt(II) structural motifs.[39,41,49,102−105] These powder patterns range across impressive breadths, with Ω values of 7250 ppm (640 kHz at 9.4 T) for $Pt(NH_3)_4Cl_2{\cdot}H_2O$ and 10420 ppm (920 kHz at 9.4 T) for K_2PtCl_4. Despite this, the use of frequency-stepped acquisition and the WURST-CPMG pulse sequence results in relatively short experimental times for both reagents (Table S4). There is a shorter recycle delay associated with $Pt(NH_3)_4Cl_2{\cdot}H_2O$ due to its shorter $T_1(^{195}Pt)$, which likely results from contributions to the longitudinal relaxation from ^{195}Pt−^{1}H dipolar couplings (from both NH_3 and mobile H_2O) which are absent in K_2PtCl_4.

At first glance, the spectrum of MGS (Figure 1c) appears to be composed of a simple superimposition of powder patterns corresponding to the individual reagents; however, the extracted CS tensors indicate otherwise. Simulations of the overall MGS powder pattern reveal that its $[Pt(NH_3)_4]^{2+}$ and $[PtCl_4]^{2-}$ units have ^{195}Pt CS tensors with significantly larger Ω and higher δ_{iso} values than those of the starting reagents. It is also noted that the Pt−Pt interlayer distances in $Pt(NH_3)_4Cl_2{\cdot}H_2O$ and K_2PtCl_4 are 4.220 and 4.144 Å, respectively,[90,91] but only 3.245 Å in MGS, inviting the preliminary hypothesis that the ^{195}Pt CS tensor is sensitive to Pt−Pt metallophilic interactions. These interactions occur perpendicular to the square plane, corresponding to the orientation of the δ_{11} component of the ^{195}Pt CS tensor (as predicted from molecular symmetry and the value of κ). Furthermore, δ_{11} is the only component that substantially differs between MGS and the starting reagents. In addition, we also note that the spectra associated with $[Pt(NH_3)_4]^{2+}$ and $[PtCl_4]^{2-}$ units in MGS are associated with distinct optimized ^{195}Pt NMR recycle delays, implying that each of the two unique Pt atoms has a disparate $T_1(^{195}Pt)$ value. This mirrors the difference in recycle delays observed in the individual starting reagents (Table S4).

Attempts were made to study MPS via WURST-CPMG using the same experimental parameters utilized in the acquisition of spectra of MGS; however, these experiments resulted in a broad powder pattern of irregular shape (Figure S3). The long relaxation delays (40 s) employed in these experiments imply that the $T_1(^{195}Pt)$ value for the $[PtCl_4]^{2-}$ unit in MPS is much longer than those of similar Pt sites in MGS and K_2PtCl_4. Since much longer relaxation delays render ^{195}Pt WURST-CPMG experiments impractical, the use of a CP experiment which relies on the much lower $T_1(^1H)$ value would be advantageous (vide infra).

^{1}H−^{195}Pt BRAIN-CP/WURST-CPMG Experiments. The recently introduced BRAIN-CP pulse sequence,[48] which is readily combined with WURST-CPMG (BRAIN-CP/WURST-CPMG), was utilized to acquire the ^{195}Pt powder pattern of MPS. These experiments offer potential S/N enhancement similar to CP, a broadband excitation similar to WURST-CPMG experiments, and a reliance on the generally shorter T_1 of the abundant nucleus (i.e., $T_1(^1H) < T_1(^{195}Pt)$ in most cases). The ^{195}Pt NMR spectrum of MPS obtained using a ^{1}H−^{195}Pt static BRAIN-CP/WURST-CPMG experiment (Figure 1d) appears to be composed of two distinct patterns, presumably corresponding to $[PtCl_4]^{2-}$ and $[Pt(NH_3)_4]^{2+}$ ions. It is important to note that the $[PtCl_4]^{2-}$ species is detected in this spectrum, confirming the presence of strong dipolar couplings between the ^{195}Pt nuclei in $[PtCl_4]^{2-}$ units and the amine protons of $[Pt(NH_3)_4]^{2+}$ units. This infers that these species are proximate and are incorporated into the unique MPS compound (i.e., this sample is clearly not just a simple heterogeneous mixture of the two starting reagents). Analogous BRAIN-CP/WURST-CPMG experiments on MGS and $Pt(NH_3)_4Cl_2{\cdot}H_2O$ (Figure 1e,f) require much shorter experimental times to obtain comparable S/N and higher resolution (Table S7).

The CS tensor parameters extracted from the ^{195}Pt powder pattern of MPS (Table 1) are almost identical to those of the corresponding K_2PtCl_4 and $Pt(NH_3)_4Cl_2{\cdot}H_2O$ reagents. In other words, although CP experiments confirm that these units are spatially proximate within MPS, Pt−Pt metallophilic interactions are not present. This suggests a longer Pt−Pt distance in MPS in comparison to MGS or perhaps the existence of some other major structural difference. Interestingly, the low-frequency portion of the MPS powder pattern, corresponding to the δ_{22}/δ_{33} components of the platinum CS tensor, is abnormally broadened in comparison to similar regions in the spectra of the individual reagents and MGS, increasing the associated uncertainties of CS tensor parameters and suggesting that this region of the powder pattern may be indicative of the presence of multiple powder patterns (and multiple Pt sites) and/or distributions of anisotropic chemical shifts arising from some degree of disorder or lack of long-range ordering. This broadening hints at additional structural information that may be contained in the powder pattern that is not resolved due to the limited resolution of the CPMG method.

^{195}Pt Hahn-Echo and ^{1}H−^{195}Pt CP-Echo NMR Experiments. In order to further investigate the δ_{22}/δ_{33} regions of the ^{195}Pt powder patterns of MPS, a series of ^{195}Pt DE Hahn-echo and ^{1}H−^{195}Pt CP Hahn-echo experiments were performed. The spectra (Figure 2) were obtained with the transmitter frequency set to the approximate center of gravity of the δ_{22}/δ_{33} region, as determined from CPMG-type experiments, in order to obtain a higher-resolution pattern that may aid in resolving the discontinuities associated with multiple, overlapping powder patterns. ^{195}Pt Hahn-echo spectra of the δ_{11} regions of all compounds were also acquired in order to extract increasingly accurate ^{195}Pt CS tensor parameters (Table 1, Figure S5). Recycle delays for Hahn-echo experiments (Table S8) were experimentally optimized to ensure full recovery of equilibrium magnetization. For $Pt(NH_3)_4Cl_2{\cdot}H_2O$, the Hahn-echo spectrum of the δ_{22}/δ_{33} region of the powder pattern reveals a single, sharp discontinuity, characteristic of a platinum CS tensor with $\kappa = -1$. For MGS, equivalent experiments reveal two distinct discontinuities at ca. −4725 and −4770 ppm, corresponding to two separate ^{195}Pt powder patterns, which are assigned to the $[Pt(NH_3)_4]^{2+}$ and $[PtCl_4]^{2-}$ species, respectively. These assignments were made according to peak intensities: the δ_{22}/δ_{33} region with highest intensity in a DE

dx.doi.org/10.1021/ja4076277 | J. Am. Chem. Soc. 2014, 136, 1333−1351

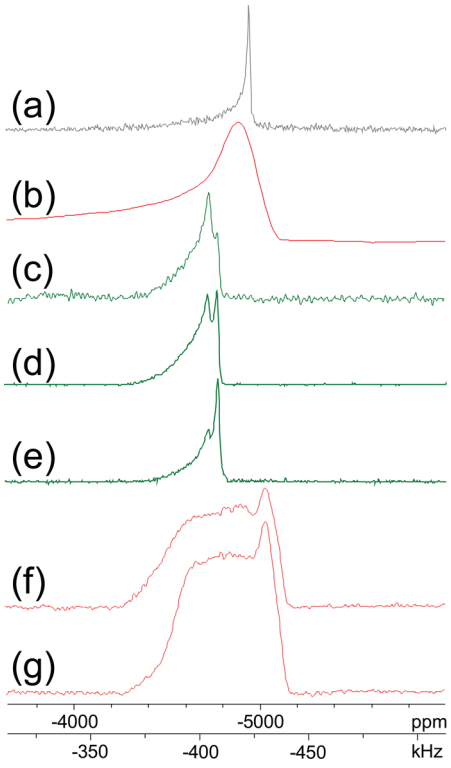

Figure 2. Individual static Hahn-echo ^{195}Pt NMR spectra (i.e., single subspectra excited by a single rectangular pulse) of (a) $Pt(NH_3)_4Cl_2 \cdot H_2O$, (b) WURST-CPMG spectrum of K_2PtCl_4 co-added in the time domain,[50] (c) Hahn-echo spectrum of MGS. ^{1}H−^{195}Pt CP-echo NMR spectra of MGS using (d) 16 and (e) 3 ms contact times as well as CP-echo NMR spectra of MPS using (f) 15 and (g) 3 ms contact times.

^{195}Pt Hahn-echo experiment arises from the $[Pt(NH_3)_4]^{2+}$ species, as it has a smaller Ω value, meaning that its powder pattern is spread over a narrower region than that of the $[PtCl_4]^{2-}$ species. Interestingly, peak intensities obtained via ^{1}H−^{195}Pt CP-echo experiments on MGS are dissimilar to those obtained via ^{195}Pt Hahn-echo experiments, the latter of which is quantitative in terms of integrated signal intensity and spin counting, provided that suitably long recycle delays are applied. Shorter ^{1}H−^{195}Pt CP mixing times are more efficient for CP to the $[PtCl_4]^{2-}$ ion, while longer mixing times are more efficient for CP to the $[Pt(NH_3)_4]^{2+}$ ion; hence, integrated signal intensities are not quantitative.

In contrast to the relatively narrow δ_{22}/δ_{33} portion of the MGS powder pattern, ^{1}H−^{195}Pt CP-echo experiments on MPS (Figure 2f,g) reveal a broad region of spectral intensity punctuated by fine structure (DE experiments were unsuccessful, vide supra). There are two major regions of spectral intensity within the δ_{22}/δ_{33} portion of the MPS powder pattern: a higher-frequency region of generally uniform intensity which stretches from ca. −4600 to −4930 ppm, and a lower-frequency region of high signal intensity from ca. −4960 to −5150 ppm. The former region encompasses the δ_{22}/δ_{33} regions of the powder patterns of both MGS and $Pt(NH_3)_4Cl_2 \cdot H_2O$, indicating their presence as minor impurities. The latter region has shifts that do not correspond to any discontinuities from the patterns of the starting reagents or MGS. This region is also abnormally broad for a single powder pattern and appears to have subtle details which may be indicative of two distinct MPS species (i.e., two ^{195}Pt CS tensors with $\kappa \approx -1$ corresponding to $[Pt(NH_3)_4]^{2+}$ and $[PtCl_4]^{2-}$ ions). There may also be a distribution of anisotropic chemical shifts arising from the main constituents and/or the impurities in the sample which also serve to broaden these regions. It is also important to note that none of the aforementioned spectral intensity in Figure 2 arises from any K_2PtCl_4 impurities in the MPS sample, as this would not be observed via ^{1}H−^{195}Pt CP experiments.

The two-site simulation of MPS (Figure 3a) does not adequately account for the uniform intensity observed in the experiment from −4600 to −4930 ppm. As described above, CP experiments are clearly not quantitative, and the intensity from −4600 to −4930 ppm in the MPS spectrum is likely due to the presence of small amounts of MGS and $Pt(NH_3)_4Cl_2 \cdot H_2O$ in the MPS sample. CP efficiency is very high for MGS and $Pt(NH_3)_4Cl_2 \cdot H_2O$ in comparison to MPS, so it is unsurprising that small amounts of these samples yield

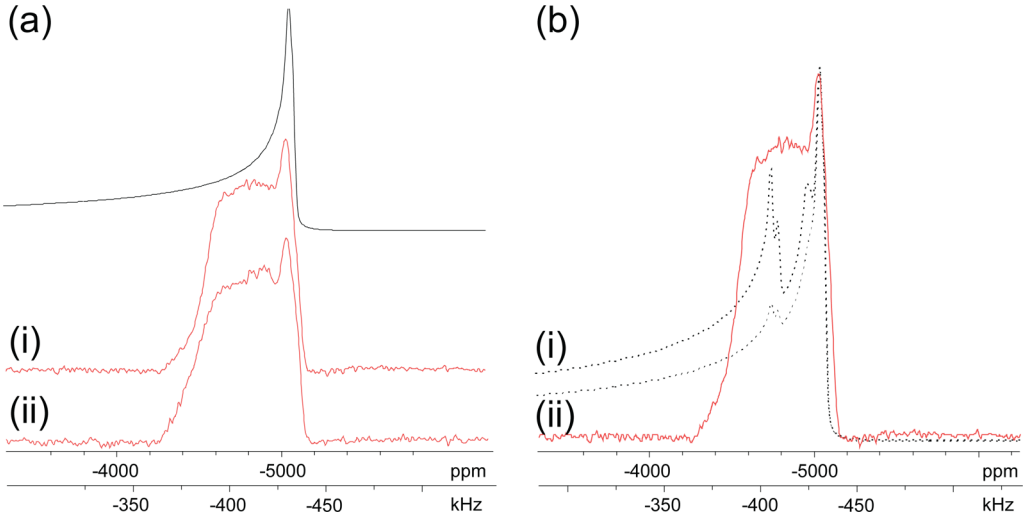

Figure 3. Individual ^{1}H−^{195}Pt CP-echo NMR spectra (i.e., single subspectra excited by a single rectangular pulse) of MPS. (a) A two-site simulation along with experimental spectra utilizing a contact time of (i) 3 ms and (ii) 15 ms. (b) Experimental spectrum (contact time of 3 ms) along with simulated spectra (dashed lines) accounting for two unique Pt sites in MPS along with $Pt(NH_3)_4Cl_2 \cdot H_2O$ and MGS impurities at relative integrated intensities of (i) 40% and (ii) 10%.

dx.doi.org/10.1021/ja4076277 | J. Am. Chem. Soc. 2014, 136, 1333−1351

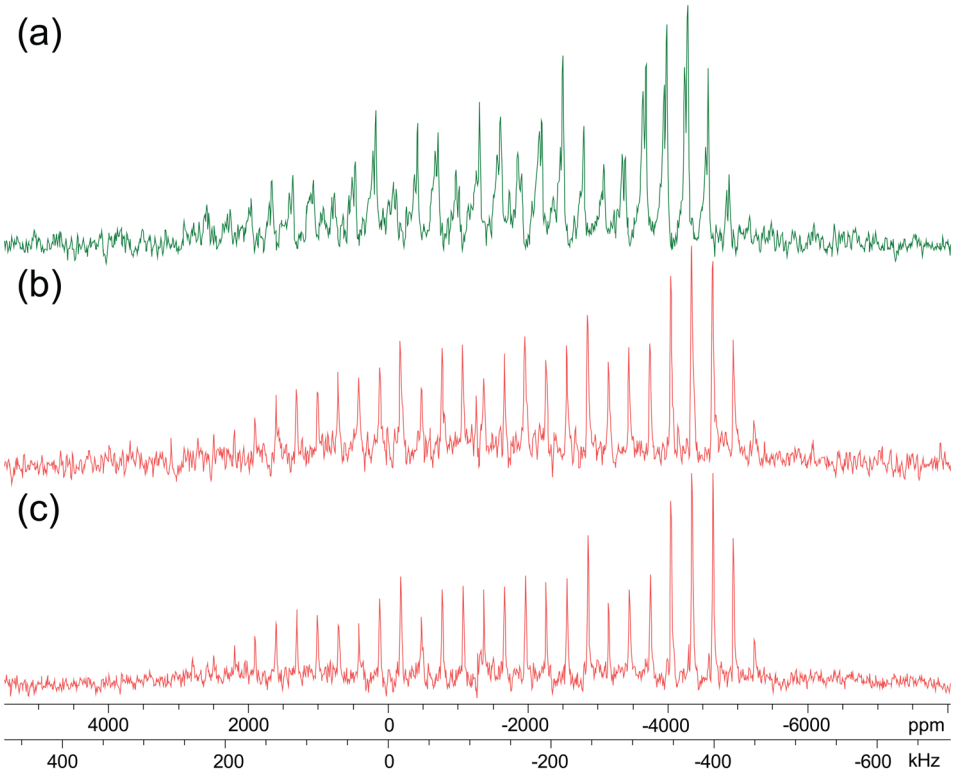

Figure 4. ^{195}Pt MAS NMR spectra of (a) MGS and (b, c) MPS. The MGS spectrum shown in (a) was acquired at a spinning speed of 25.5 kHz using a recycle delay of 40 s, while a spinning speed of 25.5 kHz and recycle delays of 90 and 8 s were used to acquire the MPS spectra depicted in (b) and (c), respectively.

significant signal intensity in the CP spectra (see Tables S9 and S10 for comparisons of CP NMR experimental times). We note that pXRD also indicates the presence of only traces of these compounds in the MPS samples (vide infra). A five-site ^{195}Pt NMR simulation (Figures 3b and S6) considering various impurities in the MPS sample is able to account for most of this unassigned spectral intensity. Since this simulation is less than perfect, the notion persists that there is some degree of disorder in this sample and corresponding broadening from distribution of chemical shifts. This is consistent with the pXRD structure of MPS, which indicates some degree of disorder (vide infra). In addition, experiments on impure MPS samples exhibit high spectral intensity in the −4600 to −4930 ppm region (Figure S7), indicating that this intensity originates from impurities and not the MPS compound itself.

^{195}Pt MAS NMR Experiments. A series of DE ^{195}Pt MAS NMR experiments were performed in order to attempt to differentiate the number and nature of Pt-containing compounds within MPS via their isotropic chemical shifts. ^{195}Pt MAS NMR spectra of MGS and MPS are shown in Figure 4. Although fast spinning speeds (ca. 25 kHz) and very short 90° pulse lengths (1 μs) were employed (Table S11), the entire manifold of spinning sidebands does not appear to be uniformly excited over its entire breadth (ca. 1 MHz at 9.4 T). In addition, S/N is very low, despite the acquisition of a large number of transients. The extraction of CS tensor parameters from these spectra is very unreliable, as previously demonstrated for ^{195}Pt and ^{207}Pb CS tensor parameters extracted from very broad MAS patterns via Herzfeld Berger analysis (HBA).[41,106] Furthermore, due to the ineffectiveness of CP at high spinning speeds, direct excitation experiments on ^{195}Pt must be applied; however, the long recycle delays and subsequent lengthy experimental times make these experiments very challenging. Despite all of this, MAS NMR experiments can be useful for identifying and refining δ_{iso} values for the individual Pt species and potentially for the detection of multiple sites.

The ^{195}Pt MAS NMR spectrum of MGS (Figure 4a) reveals two distinct sets of spinning sidebands originating from two unique Pt species. The δ_{iso} values for the $[PtCl_4]^{2-}$ and $[Pt(NH_3)_4]^{2+}$ species are unique in comparison to those of the starting reagents. We note that a calibrated recycle delay of 40 s was employed to ensure full recovery of equilibrium magnetization. The MAS spectrum of MPS (Figure 4b) has only one set of spinning sidebands corresponding to a single Pt species. The δ_{iso} of −2560(6) ppm is assigned to the $[Pt(NH_3)_4]^{2+}$ species based on CS tensor parameters extracted from BRAIN-CP/WURST-CPMG experiments (vide supra). A recycle delay of 90 s was employed in a second experiment, in an attempt to observe the $[PtCl_4]^{2-}$ species, with no success (Figure 4c). This information, paired with the failure to obtain a proper ^{195}Pt powder pattern with direct excitation WURST-CPMG experiments, suggests that the ^{195}Pt nucleus of the $[PtCl_4]^{2-}$ species of MPS has a much longer T_1 value than that of the $[PtCl_4]^{2-}$ species of MGS. The lack of a proximate source of mobile protons in MPS to induce faster ^{195}Pt longitudinal relaxation is again consistent with a major structural difference between MPS and MGS, such as a difference in the distance and/or angles between $[PtCl_4]^{2-}$ and $[Pt(NH_3)_4]^{2+}$ units.

^{14}N WURST-CPMG and ^{1}H−^{14}N BRAIN-CP/WURST-CPMG Experiments. Since three of the four compounds contain the $[Pt(NH_3)_4]^{2+}$ ion, ^{14}N SSNMR experiments were performed in an attempt to elicit additional structural information. ^{14}N is a quadrupolar nucleus with a spin of 1

dx.doi.org/10.1021/ja4076277 | J. Am. Chem. Soc. 2014, 136, 1333−1351

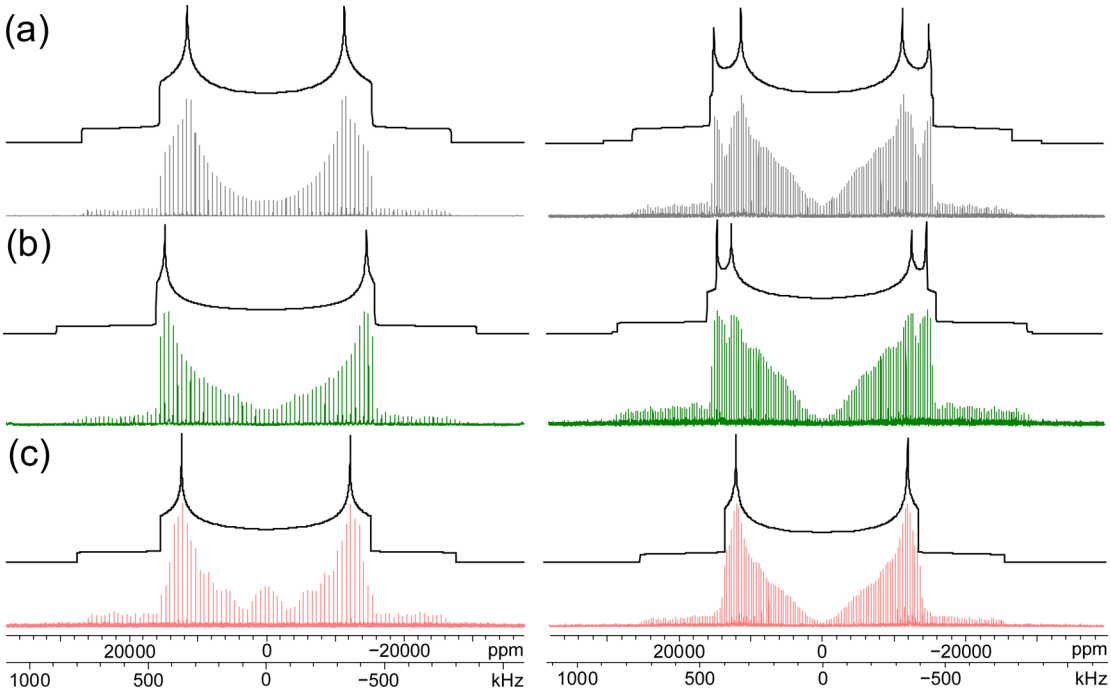

Figure 5. ^{14}N static NMR spectra (bottom traces) and simulations (top traces) of (a) $Pt(NH_3)_4Cl_2{\cdot}H_2O$, (b) MGS, and (c) MPS. Spectra on the left were acquired with direct-excitation WURST-CPMG experiments, spectra on the right were acquired using ^{1}H−^{14}N BRAIN-CP/WURST-CPMG experiments.

and is usually associated with SSNMR spectra that are dominated by the first-order quadrupolar interaction (FOQI).[107,108] In comparison to the FOQI, the effects of nitrogen CSA on ^{14}N SSNMR spectra are minimal, and no nitrogen CS tensor parameters or δ_{iso} values could be determined for these systems. However, since the powder patterns are Pake doublets with mirror symmetry, the complete ^{14}N NMR spectra were generated by "reflecting" the low-frequency (right) portion of the powder pattern about δ = 0 ppm (see Experimental section).[72]

The ^{14}N SSNMR spectra are shown in Figure 5, and the corresponding EFG tensor parameters are summarized in Table 2. Initially, ^{14}N direct-excitation WURST-CPMG experiments were performed (Figure 5, left), but unfavorably long $T_1(^{14}N)$ values resulted in long experimental times (Table S5). The lengthy experimental times also limited the resolution with which the spectra could be acquired; as a result, the accuracy of the quadrupolar parameters extracted from these spectra is questionable. ^{1}H−^{14}N BRAIN-CP/WURST-CPMG experiments were subsequently used to acquire spectra (Figure 5, right), yielding substantial increases in both S/N and spectral resolution and concomitant decreases in experimental times (Table S7) due to the relatively short $T_1(^1H)$ values. All spectra are approximately between 1500 and 1700 kHz wide at 9.4 T and exhibit well-defined features, correlating to relatively axially symmetric ^{14}N EFG tensors with η_Q values ranging from 0.02 to 0.15 and C_Q values between 1.00 and 1.20 MHz.

The most striking difference between the WURST-CPMG and BRAIN-CP/WURST-CPMG spectra are the apparent number of powder patterns arising from the $Pt(NH_3)_4Cl_2{\cdot}H_2O$ and MGS samples. WURST-CPMG experiments seem to indicate only one powder pattern for each of these compounds, while BRAIN-CP/WURST-CPMG experiments indicate that there are two distinct powder patterns for each. Both types of experiments indicate that the MPS sample gives rise to a single powder pattern. The origin of the discrepancy in observed powder patterns for $Pt(NH_3)_4Cl_2{\cdot}H_2O$ and MGS in these experiments lies in the differences in T_1 relaxation times between the two ^{14}N environments. Since only one powder pattern is observed in direct-excitation WURST-CPMG experiments, the other unobserved powder pattern must be associated with a ^{14}N environment with a much longer T_1 value. When ^{1}H−^{14}N BRAIN-CP/WURST-CPMG experiments are employed, both powder patterns are observed, owing to the reliance of these experiments on the uniformly short $T_1(^1H)$ values rather than the disparate $T_1(^{14}N)$ values.

Both the ^{14}N WURST-CPMG and the ^{1}H−^{14}N BRAIN-CP/WURST-CPMG pulse sequences produce spectra that exhibit a

Table 2. Experimental ^{14}N EFG Tensor Parameters

compound	method[a]	site (% intensity)[b]	$\lvert C_Q\rvert$ (MHz)[c]	η_Q[d]
$Pt(NH_3)_4Cl_2{\cdot}H_2O$	W		1.04(5)	0.15(5)
	BC	N1 (33)	1.19(2)	0.02(2)
	BC	N2 (100)	1.03(2)	0.15(2)
MGS	W		1.14(6)	0.04(6)
	BC	N1 (25)	1.14(2)	0.005(5)
	BC	N2 (100)	1.11(2)	0.12(2)
MPS	W		1.06(6)	0.11(6)
	BC		1.00(2)	0.07(2)

[a]W = WURST-CPMG experiment, BC = ^{1}H−^{14}N BRAIN-CP/WURST-CPMG experiment. [b]^{14}N powder patterns obtained using BRAIN-CP/WURST-CPMG require simulation using different relative intensities due to differences in ^{1}H−^{14}N cross-polarization efficiency between the two unique nitrogen environments. [c]Quadrupolar coupling constant: $C_Q = eQV_{33}/h$, where the principal components of the EFG tensor are defined as $|V_{33}| \geq |V_{22}| \geq |V_{11}|$. Only the absolute values of C_Q can be obtained from the NMR powder patterns, not their signs. [d]Asymmetry parameter: $\eta_Q = (V_{11} - V_{22})/V_{33}$.

dx.doi.org/10.1021/ja4076277 | J. Am. Chem. Soc. 2014, 136, 1333−1351

characteristic "dip" in the center of the ^{14}N powder patterns (i.e., a lack of experimental spectral intensity in comparison to the simulated idealized powder pattern). This dip is particularly pronounced in spectra produced from ^{1}H−^{14}N BRAIN-CP/WURST-CPMG experiments, where CP efficiency has been observed to decrease near the center of the Pake doublet.[109] Conversely, the ^{14}N WURST-CPMG spectrum of MPS displays a "bump" or excess of spectral intensity in the center of the powder pattern. This is partially due to low S/N of individual subspectra, owing to the short $T_2(^{14}N)$ and long $T_1(^{14}N)$ time constants and correspondingly long experimental times for ^{14}N DE NMR of MPS (Table S5). The positioning of the transmitter close to the center of the Pake doublet for the acquisition of the WURST-CPMG spectra results in increased intensity near the center of the doublet, which arises from the DEISM effect.[110] We stress that it is not crucial to obtain the spectral intensity in the centers of these symmetrical powder patterns corresponding to EFG tensors of high axial symmetry, since the ^{14}N quadrupolar parameters depend only upon the positions of the three diagnostic features (horn, shoulder, and foot), which are undistorted, well-resolved, and separated from the center of these powder patterns by relatively large frequency differences.

The ^{14}N powder patterns of $Pt(NH_3)_4Cl_2{\cdot}H_2O$ and MGS correspond to two unique, but similar, EFG tensors. As noted elsewhere, ^{14}N EFG tensors are sensitive to inter- and intramolecular hydrogen-bonding interactions involving nitrogen-bound protons,[107,111−113] and subtle differences in the strength of these interactions lead to differences in ^{14}N EFG tensor parameters. In similar square-planar Pt(II) systems containing amine groups, the EFG tensor is generally axially symmetric (i.e., $\eta_Q \approx 0$), and its principal component with the largest absolute magnitude, V_{33}, is oriented on or near the 3-fold axis of rotational symmetry (C_3 axis) coincident with the Pt−N bond, while V_{22} and V_{11} are perpendicular to this axis.[41] The C_3 rotational symmetry may be disrupted by hydrogen bonding involving amine protons, which results in a loss of axial symmetry of the EFG tensor and corresponding nonzero η_Q values.[111]

In the case of $Pt(NH_3)_4Cl_2{\cdot}H_2O$, our ab initio geometry-optimized structure (more reliable than the crystal structure, vide supra) predicts that two crystallographically unique ^{14}N sites, N1 and N2, are present due to a very subtle deviation from a D_{4h} square-planar geometry about Pt. The deviation from square-planar symmetry is slight, with ∠N1−Pt−N2 = 88.95°, ∠N2−Pt−N1 = 91.05°, torsion angle ∠N1−Pt−N2−N1 ≈1°, and difference of 0.002 Å in Pt−N1 and Pt−N2 bond length. Such differences, however, give rise to distinct N−H···Cl distances for each nitrogen site (Table S14, Figure S10). With regard to N1, the relatively shorter N1−H···Cl distances lead to hydrogen bonding which disrupts the C_3 rotational symmetry about the Pt−N1 bond, resulting in a ^{14}N EFG tensor of lower axial symmetry (higher η_Q of 0.15) compared to the tensor associated with the N2 crystallographic site (lower η_Q of 0.02).

The reported MGS crystal structure indicates one unique ^{14}N site,[27] however, it is very likely that small deviations from ideal D_{4h} square-planar symmetry are present, as in $Pt(NH_3)_4Cl_2{\cdot}H_2O$. The ^{14}N BRAIN-CP/WURST-CPMG spectrum of MGS indicates the presence of two similar ^{14}N EFG tensors, differentiated via local N−H···Cl hydrogen-bonding (η_Q values of 0.12 and 0.005). The distinction between crystallographic nitrogen sites in MGS, as represented by the ^{14}N EFG tensors, is less pronounced than in the $Pt(NH_3)_4Cl_2{\cdot}H_2O$ system, possibly owing to the nature of Cl atoms in these systems (i.e., Cl is covalently bound to Pt in MGS but is a counterion in $Pt(NH_3)_4Cl_2{\cdot}H_2O$, which may result in distinct hydrogen bonds in the latter).

The ^{14}N SSNMR spectrum of MPS displays a single powder pattern, from which values of C_Q of 1.00 MHz and η_Q of 0.07 are determined. The ^{14}N EFG tensor parameters of the ^{14}N sites in MPS are similar to the compounds discussed previously and indicate that the $[Pt(NH_3)_4]^{2+}$ ion is intact within MPS. The absence of a distinct second ^{14}N powder pattern provides clear evidence that the structure of MPS is quite different from that of $Pt(NH_3)_4Cl_2{\cdot}H_2O$ and MGS and that any deviations from D_{4h} symmetry in the $[Pt(NH_3)_4]^{2+}$ species within MPS must be extremely small. The MPS ^{14}N EFG tensor displays a nonzero η_Q value that, when compared to MGS and $Pt(NH_3)_4Cl_2{\cdot}H_2O$ ^{14}N EFG tensors, suggests that amine groups in MPS may be involved in hydrogen bonding with nearby Cl atoms (as in the case of the site N2 nitrogens in $Pt(NH_3)_4Cl_2{\cdot}H_2O$). Perhaps most importantly, both the ^{14}N and ^{195}Pt NMR data suggest that the long-range structure of MPS is different from those of MGS and the starting reagents and that there may be very different unit cell parameters and space group symmetry.

^{35}Cl WURST-CPMG Experiments. In order to verify the presence of $[PtCl_4]^{2-}$ units within MPS and investigate their local environments, ^{35}Cl SSNMR experiments were performed on all of the Pt complexes. There are two NMR active chlorine isotopes, ^{35}Cl and ^{37}Cl, which both have nuclear spins of $I = 3/2$, moderately sized nuclear quadrupole moments, and relatively low gyromagnetic ratios (they are classified as low-γ nuclides). The former is generally preferred for SSNMR studies, due to its higher natural abundance. ^{35}Cl SSNMR powder patterns are typically dominated by the second-order quadrupolar interaction (SOQI), whose nature depends solely on the electric field gradients (EFG) about the ^{35}Cl nucleus; however, for narrower patterns arising from smaller C_Q values, the effects of chlorine chemical shift anisotropy (CSA) can often be observed. The breadth of the central transition (CT) of the ^{35}Cl SSNMR pattern scales inversely with magnetic field; hence, it is advantageous to utilize a field of 21.1 T for all ^{35}Cl NMR experiments. The majority of reports on ^{35}Cl SSNMR have dealt with ionic chlorine species with relatively narrow patterns and correspondingly small nuclear quadrupolar coupling constants, C_Q.[64,114−118] Recently, ^{35}Cl UW NMR experiments have been applied to study chlorine atoms in terminal and bridging bonding environments in transition-metal complexes as well as in terminal carbon−chlorine bonds in organic molecules, where powder patterns can be over several MHz in breadth.[41,63,119−123]

The ^{35}Cl SSNMR spectra for all compounds are shown in Figure 6, and the corresponding EFG tensor parameters are presented in Table 3. The ^{35}Cl NMR powder pattern for $Pt(NH_3)_4Cl_2{\cdot}H_2O$ (Figure 6b) is very narrow in comparison to those of all the other systems and arises from a single unique site. The Cl^- ions in $Pt(NH_3)_4Cl_2{\cdot}H_2O$ are not involved in any covalent bonds; hence, ^{35}Cl nuclei in such environments experience small EFGs and, correspondingly, have small C_Q values. The remainder of the systems have very broad patterns and large values of C_Q, since the Cl atoms therein are involved in covalent bonds. Since the magnitude of the quadrupolar interactions in these systems is very large in comparison to the spans of the chemical shift (CS) tensors, it is impossible to

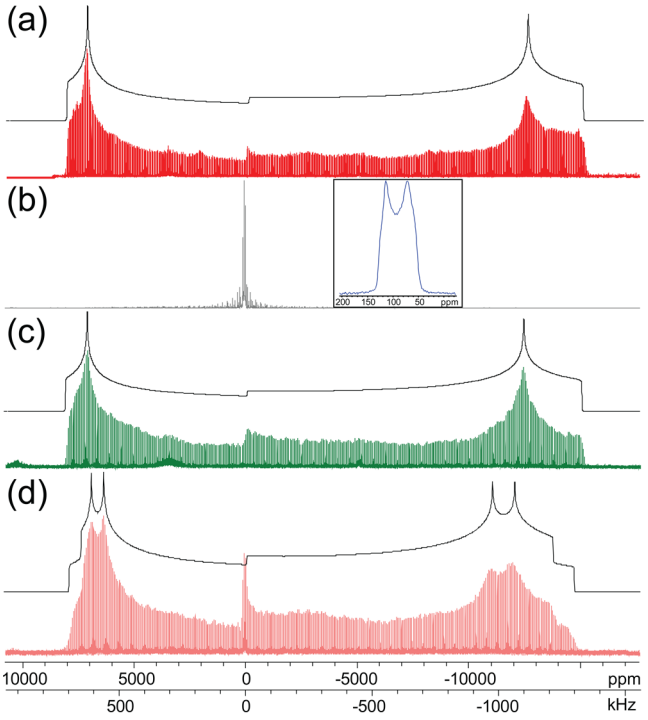

Figure 6. Static WURST-CPMG ^{35}Cl NMR spectra acquired at 21.1 T (bottom traces) and simulations (top traces) of (a) K_2PtCl_4, (b) $Pt(NH_3)_4Cl_2{\cdot}H_2O$ (with Hahn-echo experiment inset), (c) MGS, and (d) MPS.

Table 3. Experimental ^{35}Cl NMR Parameters[a]

compound	site	$\lvert C_Q \rvert$ (MHz)[b,c,d]	η_Q[c,d]	δ_{iso} (ppm)
K_2PtCl_4		35.7(2)	0.09(1)	−125(75)
$Pt(NH_3)_4Cl_2{\cdot}H_2O$		1.85(5)	0.30(5)	100(5)
MGS		35.6(2)	0.095(10)	−125(75)
MPS	1	33.8(2)	0.11(1)	0(75)
	2	35.1(1)	0.10(1)	0(75)

[a]All ^{35}Cl NMR experiments were conducted at a magnetic field strength of 21.1 T. $Pt(NH_3)_4Cl_2{\cdot}H_2O$ was acquired using a Hahn-echo pulse sequence, all other spectra were acquired using the WURST-CPMG pulse sequence. [b]These ^{35}Cl spectra are dominated by the second-order quadrupolar interaction, making quantification of the relatively smaller contributions from the chlorine CSA impossible in all cases. [c,d]See definitions given in footnotes *c* and *d* in Table 2.

extract any ^{35}Cl CS tensor information except for very rough estimates of δ_{iso}, even when utilizing a traditional Hahn-echo experiment.

The ^{35}Cl SSNMR spectra of K_2PtCl_4 and MGS yield EFG tensor parameters that are identical within experimental uncertainty, indicating that their respective $[PtCl_4]^{2-}$ units reside in similar environments (i.e., distinct Pt−Pt metallophilic interactions do not drastically alter the electronic structure of the Pt−Cl bonds). In agreement with their reported crystal structures, the $[PtCl_4]^{2-}$ units within K_2PtCl_4 and MGS each give rise to a single ^{35}Cl powder pattern.

The ^{35}Cl powder pattern of MPS has two unique powder patterns (1:1 integrated intensity ratio), both with EFG tensors similar to those of K_2PtCl_4 and MGS. The sharp resonance at ca. 100 ppm is attributed to a small amount of $Pt(NH_3)_4Cl_2{\cdot}H_2O$ reagent. The spectral features in this spectrum are not as sharp as in those of MGS and K_2PtCl_4. This may indicate a slightly lower degree of crystallinity within the MPS sample (which would result in a broadening arising from a distribution of quadrupolar parameters) or minor contamination from the MGS coproduct and K_2PtCl_4 reagent (both of these are suggested by ^{195}Pt SSNMR spectra); however, the presence of impurities is not evident in the ^{35}Cl SSNMR spectrum of MPS, suggesting that distributions of anisotropic quadrupolar parameters arising from disorder are more likely. As an illustration of the sensitivity of ^{35}Cl SSNMR to impurities in the MPS system, the ^{35}Cl SSNMR spectrum of an impure sample yields one narrow and three broad powder patterns, readily indicating the presence of MGS, K_2PtCl_4, and $Pt(NH_3)_4Cl_2{\cdot}H_2O$ impurities (Figure S11).

The columnar structures of K_2PtCl_4 and MGS give rise to a single ^{35}Cl SSNMR powder pattern, indicative of a sole ^{35}Cl crystallographic site, while spectra of MPS indicate two ^{35}Cl sites. The existence of two unique yet similar chlorine sites in MPS may be due to a subtle shift away from idealized symmetry about the $[PtCl_4]^{2-}$ square-planar center or some other structural difference. These data, along with ^{195}Pt and ^{14}N results, further suggest a MPS structure that is distinct from the common columnar or stacked square-planar Pt motif.

X-ray Absorption Fine Structure Experiments. X-ray absorption fine structure experiments were employed to probe the identity and coordination of Pt ligands in MPS. The reader is directed to the Supporting Information, Appendix A, for detailed data and accompanying figures regarding XANES and EXAFS experiments; herein only key findings are briefly discussed. XANES spectra of the Pt complexes have the same position for the absorption edge, which indicates that the Pt atoms in both MPS and MGS are of the same oxidation state as $Pt(NH_3)_4Cl_2{\cdot}H_2O$, which was used as a reference. The EXAFS analysis provides information regarding the local environment of Pt in MPS, with specific focus on ligand coordination to Pt. The fitting results of the Pt L_{III} edge confirm the presence of Pt−N and Pt−Cl bonds in MPS and indicate bond lengths of 2.032(0.013) and 2.300(0.007) Å, respectively; these bond lengths are similar to the 2.036(0.020) and 2.310(0.010) Å obtained from a sample of MGS.

Powder X-ray Diffraction Experiments, Refinement of MPS Data Guided by First Principles Calculations, and Proposed Structural Model of MPS. To further investigate the unique MPS structure suggested by SSNMR and XANES/EXAFS experiments, pXRD patterns were acquired for all compounds (Figure 7). Powder XRD experiments were completed at Beamline X7B of Brookhaven National Laboratory using a synchrotron source. The sharp peaks in each diffraction pattern are consistent with highly crystalline samples, although the slightly broader peaks in the pattern of MPS infer a lower degree of crystallinity, consistent with NMR observations. The powder patterns obtained for K_2PtCl_4, $Pt(NH_3)_4Cl_2{\cdot}H_2O$, and MGS agree well with calculated powder patterns based on reported crystal structures (Figure S12, Table S15). The powder diffraction patterns for the MPS samples clearly indicate that MPS is the major product of our synthesis, with minor peaks (i.e., $2\theta \approx 3°$) corresponding to MGS and small amounts of the starting reagents. Two separate batches of MPS were analyzed; multinuclear NMR spectra and pXRD patterns indicate that MGS and reagents are limited to minor impurities in both samples, demonstrating the reproducibility of our synthesis.

A summary of the procedure involved to establish an accurate Rietveld refinement of the pXRD data of MPS is described below and depicted in Figure 8. The reader is

dx.doi.org/10.1021/ja4076277 | J. Am. Chem. Soc. 2014, 136, 1333−1351

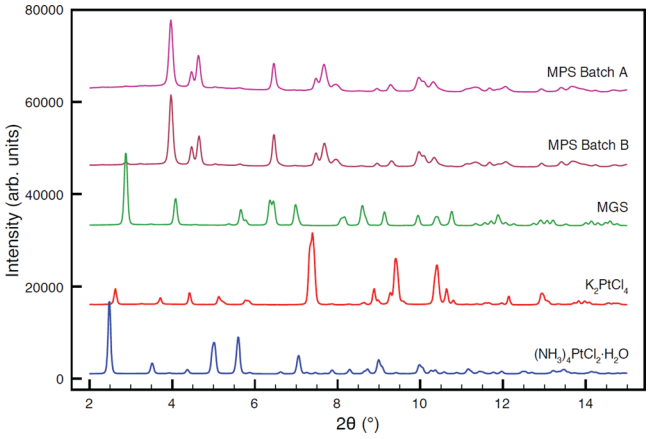

Figure 7. Powder X-ray diffraction patterns of square-planar Pt complexes. Two separate batches of MPS product were studied in order to assess the reliability of the synthesis.

directed to Appendix B of the Supporting Information for a detailed description of this protocol, including intermediate and discarded structural models. Preliminary Rietveld refinements were attempted on MPS X-ray diffraction data without success, due to the relatively low crystallinity of the MPS samples, presence of multiple trace impurities, and corresponding reduced resolution of high-angle diffraction peaks. Since Pt is associated with >90% of electron density within MPS, Pt atomic positions and unit cell dimensions were readily extracted from a Lebail fitting. Attempts to incorporate Cl or N positions resulted in no appreciable increase in fit accuracy, however, ^{195}Pt, ^{35}Cl, and ^{14}N SSNMR data were used in conjunction with pXRD results in order to formulate a preliminary structural model of MPS (Figure 8a). The most glaring flaw with this preliminary model is an impossibly short 2.300 Å Cl−Cl intermolecular distance between neighboring $[PtCl_4]^{2-}$ units. First principles geometry optimization calculations on this preliminary structure were then performed, both with and without symmetry restrictions, producing the structures depicted in Figure 8b. A blend of these geometry optimized structures was then used as the starting point for a successful Rietveld refinement of the MPS pXRD data (Figures 8c and 9),

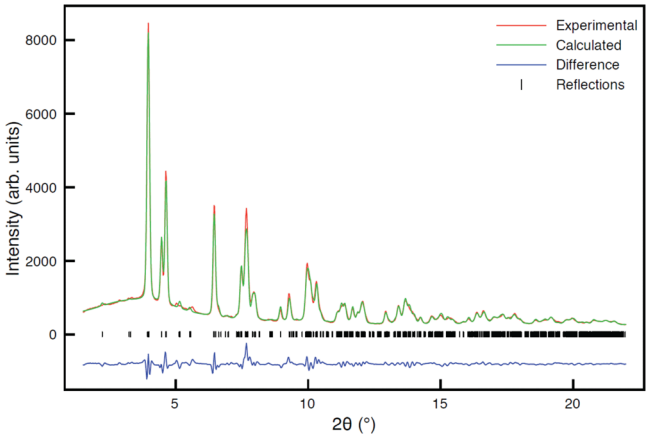

Figure 9. Rietveld refinement of MPS pXRD data using the parameters described in Table 4.

which yields all unit cell parameters and atomic positions of MPS (Figure 10, Table 4) and agrees strongly with SSNMR and EXAFS results. This refined structure was verified via a lack of significant change in atomic coordinates upon geometry optimization.

MPS displays *P*-1 symmetry and resides in a pseudotetragonal unit cell. The Rietveld refinement statistics (Table 4, footnote) of this structure are clearly superior to the initial

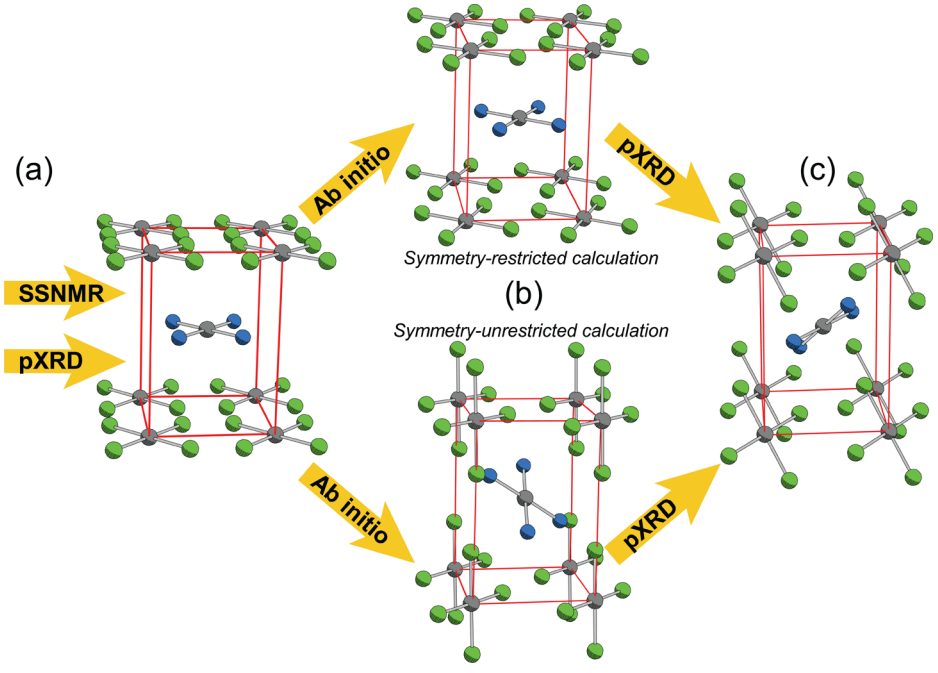

Figure 8. Flowchart of the protocol used to elucidate the crystal structure of MPS. A Lebail fitting of pXRD data combined with an initial "best guess" from SSNMR and EXAFS data produced (a), first principles geometry optimizations of this structure resulted in the two structures depicted in (b), and a Rietveld refinement of experimental pXRD data, using a combination of both structures in (b) as a starting point, resulted in the final structure of MPS depicted in (c).

dx.doi.org/10.1021/ja4076277 | *J. Am. Chem. Soc.* 2014, 136, 1333−1351

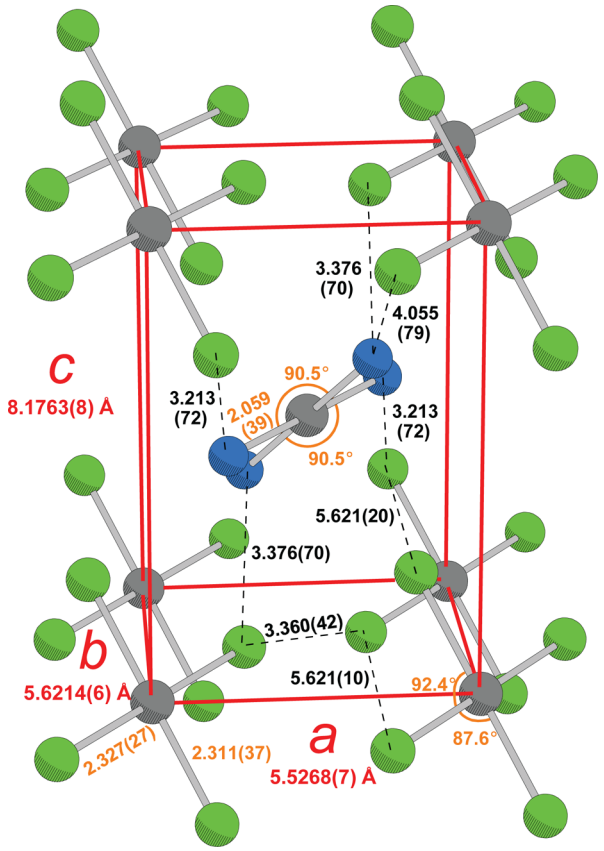

Figure 10. Structural model of MPS, generated from a Rietveld refinement of pXRD data and guided by first principles calculations. The unit cell and its dimensions are superimposed in red, while key bond distances and angles are marked in orange. All distances are listed in Å. Hydrogen atoms are omitted for clarity. Distances not shown: an intermolecular N–N distance of 3.832 Å between $[Pt(NH_3)_4]^{2+}$ units.

Table 4. Fractional Coordinates and Displacement Parameters of Atoms in MPS[a]

atom	*x*	*y*	*z*	U_{iso}
Pt1	0	0	0	0.0155(3)
Pt2	1/2	1/2	1/2	0.0155(3)
Cl1	0.2928(13)	0.2900(13)	0.0408(25)	0.0155(3)
Cl2	0.8144(20)	0.1379(25)	0.2343(8)	0.0155(3)
N1	0.2433(15)	0.2386(14)	0.4720(50)	0.0155(3)
N2	0.6849(20)	0.2905(18)	0.6646(11)	0.0155(3)

[a]Structural parameters for MPS: Space group *P*-1 (no. 2). Lattice parameters: a = 5.5268(7) Å, b = 5.6214(6) Å, c = 8.1763(8) Å, α = 89.92(4)°, β = 89.80(3)°, γ = 89.78(2)°, V = 254.02(5) Å^3, Z = 2. Fitting parameters: χ^2 = 2.407, wR_p = 5.87%, and R_p = 4.52%

Lebail fitting of Pt positions (Table B1 in Appendix B of the Supporting Information). There are no obvious flaws with this structure in terms of sterics; MPS lacks close Cl–Cl or N–N distances since the $[PtCl_4]^{2-}$ units do not reside on the crystallographic *ab* plane and the $[Pt(NH_3)_4]^{2+}$ units are not parallel to $[PtCl_4]^{2-}$. In contrast to K_2PtCl_4, $Pt(NH_4)_3Cl_2{\cdot}H_2O$, and MGS, MPS features $[Pt(NH_3)_4]^{2+}$ and $[PtCl_4]^{2-}$ units which are almost perpendicular to each other, rather than parallel. MPS also features a distance of >5.5 Å between any two square-planar Pt units. The long Pt–Pt distances, combined with nonparallel orientation of Pt square planes, clearly prohibit Pt–Pt metallophilic interactions within MPS. Every $[PtCl_4]^{2-}$ ligand participates in hydrogen bonding with nearby amine groups (Figure 10), giving rise to network of hydrogen/halogen bonding throughout the structure of MPS. The closest Cl–N distances are ca. 3.2 - 3.4 Å, and the closest H–Cl distances are estimated to be ca. 2.1 Å from first principles calculations (Figure B13).

The structure of MPS allows for new insight into the SSNMR results. All of the Pt atoms within MPS reside in isolated $[PtCl_4]^{2-}$ and $[Pt(NH_4)_3]^{2+}$ units and are not involved in metallophilic interactions, which explains the remarkable similarities between the ^{195}Pt SSNMR spectra of K_2PtCl_4, $Pt(NH_3)_4Cl_2{\cdot}H_2O$, and MPS. The only interaction involving Pt is a distant Pt···H contact of ca. 3.1 Å (Figure B13) which does not appear to impact the platinum CS tensor parameters, but acts as a source of relatively strong ^{1}H–^{195}Pt dipolar couplings which are essential for ^{1}H–^{195}Pt BRAIN-CP/WURST-CPMG experiments. The ^{14}N WURST-CPMG and ^{1}H–^{14}N BRAIN-CP/WURST-CPMG SSNMR spectra of MPS both display a single powder pattern, unlike the two patterns observed from $Pt(NH_3)_4Cl_2{\cdot}H_2O$ and MGS, due to the extensive hydrogen-/halogen-bonding network within MPS. There are two sets of crystallographically distinct (yet very similar) N atoms in MPS, but since every amine group is intimately involved in multiple hydrogen bonds of significant strength with nearby Cl ligands, all N atoms reside in approximately the same electronic environment with similar relaxation (i.e., T_1) times. Lastly, it is now evident that the two similar powder patterns observed in the ^{35}Cl SSNMR spectrum of MPS are due to a slight deviation of the $[PtCl_4]^{2-}$ units from ideal square-planar symmetry. MPS features two crystallographically unique Cl sites, both participating in hydrogen-bonding interactions, with individual Pt–Cl bond lengths of 2.327(27) and 2.311(37) Å. The Rietveld refinement also indicates a deviation in ∠Cl–Pt–Cl of about 2.5° from ideal square-planar symmetry (Figure 10). These subtle variations in Pt–Cl bond length and deformations in molecular geometry give rise to distinct EFG tensor parameters for each Cl site and explain the observation of two similar powder patterns in the ^{35}Cl SSNMR spectrum of MPS.

With a structural determination of MPS complete, computations on a selection of platinum compounds should be able to provide further insight into the experimental ^{195}Pt CS tensor parameters.

First Principles Calculations. In this section, results from DFT calculations of platinum nuclear MS tensors are presented for several model cluster compounds for $Pt(NH_3)_4Cl_2{\cdot}H_2O$, K_2PtCl_4 and MGS. As discussed in the Experimental section, calculations on MPS are excluded from the current work, due to difficulties in obtaining a molecular cluster that yielded a satisfactorily converged ground state. Model clusters (Figure 11) were constructed from atomic coordinates based on known crystal structures; geometry optimizations of the atomic positions were performed with periodic boundary conditions, as described in the Experimental section.

The platinum isotropic nuclear shielding constants, σ_{iso}, calculated with scalar (SC) and spin–orbit (SO) ZORA methods are collected in Table 5. The relative CS and MS values are given in Table 6. Examination of the differences in δ_{iso} and σ_{iso} among the various species in Table 6 reveals that the SO calculations provide slightly better quantitative agreement with experiment. This is especially clear in comparing the data for the two possible structural models for

dx.doi.org/10.1021/ja4076277 | J. Am. Chem. Soc. 2014, 136, 1333–1351

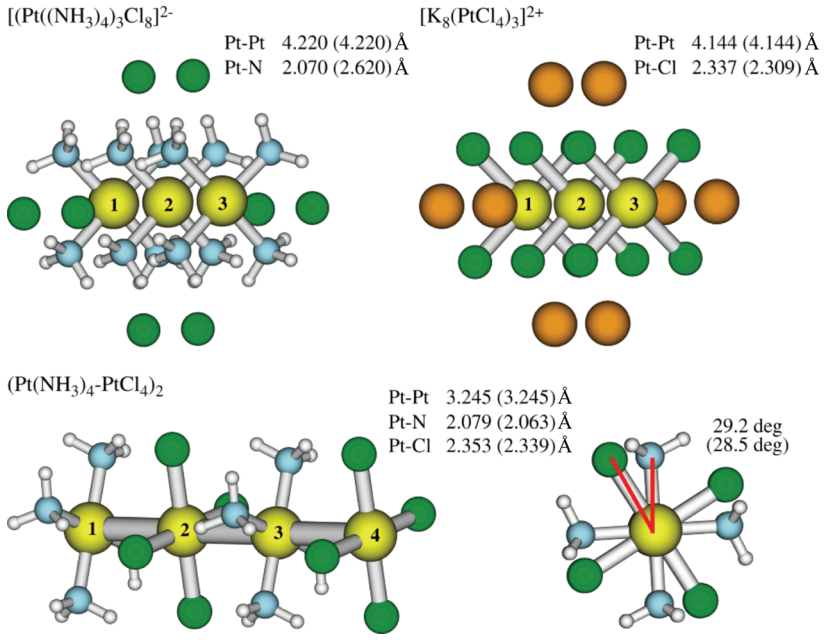

Figure 11. Molecular clusters used in the NMR calculations. The numbers listed correspond to calculated (experimental) geometric parameters.

Table 5. Calculated ZORA ^{195}Pt Isotropic Shielding and Experimental Chemical Shifts for MGS and Reagents

				calcd: PBE0/QZ4P/TZP		
				σ_{iso} (ppm)		$\Delta\sigma_{iso}$[c] (ppm)
label	system	Pt label[a]	expt δ_{iso} (ppm)[b]	SC	SO	SO−SC
A	$[(Pt(NH_3)_4)_3Cl_8]^{2-}$	2	−2507(10)	471	4034	3563
B[d]	$[K_8(PtCl_4)_3]^{2+}$	2	−1510(60)	−1401	2231	3632
B′[e]	$[K_8(PtCl_4)_3]^{2+}$	2		−690	2845	3536
C	MGS $Pt(NH_3)_4^{2+}$	3	−2208(6)	−225	3515	3740
D	MGS $PtCl_4^{2-}$	2	−970(6)	−1555	2247	3802

[a]Label of the Pt center, see Figure 11. [b]δ_{iso} values of A, C, D were taken from MAS experiments, and δ_{iso} values of B/B′ from WURST-CPMG experiments. [c]$\Delta\sigma_{iso} = \sigma_{iso}(SO) - \sigma_{iso}(SC)$. [d]Optimized structure, Pt−Cl: 2.337 Å. [e]X-ray crystal structure, Pt−Cl: 2.309 Å

Table 6. ^{195}Pt NMR Comparison of MGS and Reagents

X vs Y[a]	expt $\Delta\delta_{iso}$ (X−Y) (ppm)[b]	SC $\Delta\sigma_{iso}$ (Y−X) (ppm)[c]	SO $\Delta\sigma_{iso}$ (Y−X) (ppm)[c]
A vs B	−997	−1871	−1802
A vs B′		−1161	−1188
C vs D	−1238	−1330	−1269
A vs C	−299	−695	−519
B vs D	−540	−154	15
B′ vs D		−865	−599

[a]Labels according to Table 5. [b]$\Delta\delta_{iso}$ (X−Y) = δ_{iso}(X) − δ_{iso}(Y). [c]$\Delta\sigma_{iso}$ (Y−X) = σ_{iso}(Y) − σ_{iso}(X). Note that the order of subtraction (i.e., X−Y vs Y−X) changes between columns due to the conventions (δ vs σ) of the chemical shift and magnetic shielding scales.

K_2PtCl_4: both have the $[K_8(PtCl_4)_3]^{2+}$ cluster but feature slightly different Pt−Cl bond lengths (model **B**: 2.337 Å (geometry optimized value), model **B′**: 2.309 Å (crystal structure)).[91] In particular, the **B′** model yields differences in σ_{iso} that are closer to the experimental δ_{iso} differences. The variation in σ_{iso} resulting from the small changes in Pt−Cl bond lengths is unsurprising, as this has been previously observed in similar calculations on Pt model compounds.[81,83]

The platinum MS tensor components for the cluster models are given in Table 7. Comparison of the spans of the CS and MS tensors also shows good quantitative agreement; interestingly, the results for the **B** cluster are superior to those of **B′** in this case. The skews of each tensor are all near or equal to −1.0 (i.e., σ_{11} is distinct and $\sigma_{22} \approx \sigma_{33}$), in good agreement with experimental data. Polar plots of the anisotropic MS tensors for K_2PtCl_4 and the $PtCl_4^{2-}$ unit of MGS (Figure 12) feature blue and orange regions indicating directions of positive and negative magnetic shielding, respectively. The surfaces show the magnetic shielding response magnitude as a function of the magnetic field direction and indicate the magnitude, sign, and orientation of the tensor principal components:[124,125] hence, σ_{11} is oriented perpendicular to the square plane, and σ_{22} and σ_{33} are contained within the square plane, consistent with our arguments based on the experimental CS tensors and local symmetry of each Pt site. The MS tensors in the $Pt(NH_3)_4^{2+}$ units are similarly oriented (Figure S13). Perhaps most importantly, it is the σ_{11}/δ_{11} parameters that show the strongest differences with structural

dx.doi.org/10.1021/ja4076277 | J. Am. Chem. Soc. 2014, 136, 1333−1351

Table 7. Calculated SC and SO ZORA ^{195}Pt Shielding Tensors for MGS and Reagents[a]

		ZORA calculations					experimental	
		σ_{11}	σ_{22}	σ_{33}	Ω	κ	Ω	κ
A	SC	−3893	2590	2714	6483	−0.98	7200(50)	−0.995(5)
	SO	−462	6228	6335	6797	−0.97		
B	SC	−8358	2077	2079	10435	−1	10420(100)	−0.97(1)
	SO	−4438	5564	5568	10006	−1		
B′[b]	SC	−6939	2432	2436	9370	−1	10420(100)	−0.97(1)
	SO	−3121	5826	5831	8952	−1		
C	SC	−4930	2133	2133	7063	−1	7560(30)	−1.00(1)
	SO	−1265	5909	5909	7174	−1		
D[b]	SC	−8519	1939	1939	10458	−1	10575(50)	−1.00(1)
	SO	−4571	5666	5666	10237	−1		

[a] σ and Ω are given in ppm, κ is dimensionless. Labeling scheme according to Table 5. Calculated results of C and D obtained with linear dependency criterion of 10^{-5} au. [b] See Figure 12 for graphical representation.

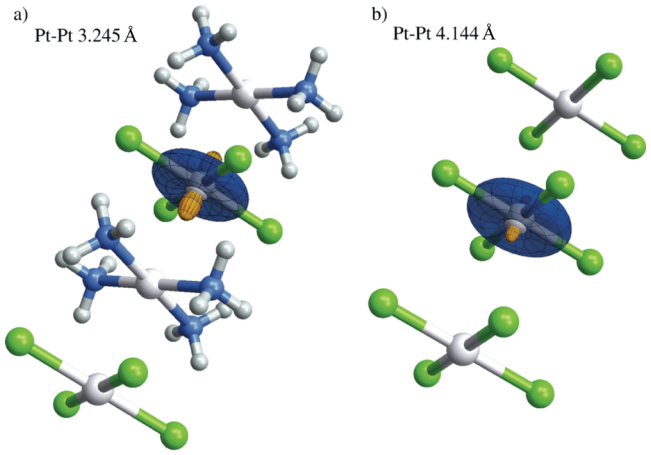

Figure 12. Graphical representations of the direction-dependent platinum shielding in (a) MGS and (b) K_2PtCl_4. Blue and orange indicate positive and negative shielding, respectively. Polar plots of the shielding tensors are scaled to 0.025 pm/ppm.

variation. Notably, decreases in Pt−Pt distances in the "columnar" complexes (i.e., the starting reagents and MGS) correspond to decreased (more negative) shielding along the direction of σ_{11}/δ_{11} (i.e., the direction of the Pt−Pt interactions).

It is of great importance to understand the relationships between differences in electronic structure and the platinum MS parameters. The results of a localized molecular orbital (LMO) analysis of platinum magnetic shielding are presented in Tables 8 and S16−18. There are three main classes of LMOs under consideration: Pt nonbonding 5d orbitals (referred to in Table 8 as "lone pairs" (LPs)), Pt-ligand σ bonds, and Pt core (CR) orbitals. It has previously been shown that it is the 5d orbitals that cause the largest variations in MS in Pt(II) versus Pt(IV) complexes.[82] They may also outweigh the latter two classes of LMOs in determining the trends in MS among Pt systems of a given oxidation state. This is precisely the case for our samples. The analysis shows that the contributions to platinum MS from other distant Pt atoms and the counterions (where applicable) are minimal.

The first four rows of Table 8 list the sum totals of contributions to σ_{iso} from LMOs centered on the central Pt units of the clusters considered (Figure 11), unoccupied LMOs, and orbitals localized on the counterions and remaining Pt units, respectively. The two columns furthest to the right show the differences in MS between the $Pt(NH_3)_4^{2+}$ and $PtCl_4^{2-}$ units in MGS and the starting reagents, respectively. It is clear

Table 8. Magnetic Shielding Analysis (in ppm) in Terms of LMOs for MGS and Reagents[a]

	$[(Pt(NH_3)_4)_3Cl_8]^{2-}$	$[K_8(PtCl_4)_3]^{2+}$ [b]	MGS $Pt(NH_3)_4^{2+}$	MGS $PtCl_4^{2-}$	Δ $Pt(NH_3)_4^{2+}$ [c]	Δ $PtCl_4^{2-}$ [c]
∑ Pt	4511	3202	4000	2651	−511	−551
∑ unocc.	−481	−331	−391	−351	90	−20
∑ counterion	9	−9	n/a	n/a	n/a	n/a
∑ other Pt moieties	−6	−16	−91	−46	n/a	n/a
∑ Pt CR	11598	11985	11583	11998	−15	13
∑ σ(Pt-ligand)	−708	−856	−583	−796	125	60
∑ ligand	56	−9	113	−16	57	−7
Pt d_{xy}	−3649	−4676	−4016	−5101	−367	−425
Pt d_{xz}, d_{yz}	−2811	−3151	−3359	−3639	−548	−488
Pt d_{z^2}	25	−91	263	206	238	297
∑ Pt LP	−6435	−7919	−7112	−8534	−677	−615
σ_{iso}	4034	2845	3518	2254	−516	−591

[a] SO ZORA computations and breakdown in terms of "natural" localized molecular orbitals obtained from the NBO program for the corresponding scalar relativistic system (see Experimental section and ref 82). Separate contributions for all the Pt units, counterion, and variational SO term (∑ unocc.) together with contributions from core (CR), Pt-ligand σ bonds, ligand and Pt 5d LP LMOs for the central Pt unit of the cluster (Figure 11) are given. The first three columns refer to Pt(2) of the corresponding cluster in Figure 11, the fourth column refers to Pt(3). All values are listed in ppm. [b] **B′** system, X-ray crystal structure, Pt−Cl: 2.309 Å. Optimized geometries used otherwise. [c] Calculated: difference between MGS and reference. The z axis is parallel to σ_{11} of the MS tensor.

dx.doi.org/10.1021/ja4076277 | J. Am. Chem. Soc. 2014, 136, 1333−1351

that the contributions from Pt-centered LMOs dominate; these are broken down and listed in the second portion of the table (rows 5−11) in terms of Pt core MOs, Pt-ligand bonding, ligand-centered, and nonbonding 5d Pt orbitals (LPs).

The d_{xy}, d_{xz}, and d_{yz} orbitals account for the largest contributions to deshielding of the Pt nuclei in the $Pt(NH_3)_4^{2+}$ and $PtCl_4^{2-}$ species of the starting reagents and even more so for MGS. The d_{z^2} orbital is responsible for moderately large shielding contributions for both species in MGS and relatively minor contributions for the starting reagents. The overall result is a larger net deshielding of the ^{195}Pt nuclei in both the $Pt(NH_3)_4^{2+}$ and $PtCl_4^{2-}$ moieties in MGS with respect to the starting reagents.

In previous work, it was shown that large differences in the Pt shielding between square-planar Pt(II) and octahedral Pt(IV) complexes can be traced back to the paramagnetic current density induced by the external field in the Pt 5d shell, which causes Pt deshielding of thousands of ppm in magnitude.[82] We adopt an "orbital rotation model" for d orbitals for the following discussion.[82,126] The major MS contribution of the d_{xy} orbital (assumed to be in-plane in this case) in comparison to all of the other orbitals can be understood by considering the effects of a "rotation" caused by the perturbation by an external magnetic field along the z-direction (for diagrams of the canonical 5d Pt orbitals, see Figure S14). In particular, a rotated d_{xy} orbital overlaps and can therefore mix with unoccupied equatorial (in-plane) σ^* orbitals (antibonding, Pt-ligand LMOs), producing the only very large deshielding contribution along the z-direction (also the direction of σ_{11}/δ_{11}, Table S17). The d_{xz} and d_{yz} orbitals are rotated in a similar manner by magnetic fields pointing along the y- and x-directions of the molecular frame, respectively; however, only two of the lobes in each case align with equatorial σ^* orbitals, while the other two lobes do not (N.B., the other magnetic field components result in rotated orbitals of π and δ symmetry with respect to the ligands; contributions to the MS from mixings involving such orbitals are small in σ-bonded Pt complexes). Individually, the contributions to deshielding of the d_{xz} and d_{yz} orbitals are less than half that of the d_{xy} orbital and are directed within the square plane (Table S18). Interestingly, these deshielding contributions are partially "counteracted" by shielding contributions involving rotation of the d_{z^2} orbital by the same magnetic fields (Tables S17, S18).

The in-plane (σ_{22}, σ_{33}) as well as the out-of-plane (σ_{11}) MS tensor components are more negative in MGS (more deshielded) than in the starting reagents. This applies to both the $PtCl_4^{2-}$ and the $Pt(NH_3)_4^{2+}$ moieties in MGS. Individually, the σ_{11} tensor components are most strongly altered in MGS compared to the starting reagents. Tables S17 and S18 show that the more negative σ_{11} and the more negative σ_{22}, σ_{33} all contribute negative several hundred ppm to the more deshielded isotropic MS. The LMO analysis shows that the increased deshielding in MGS does not result from major contributions from anything other than the Pt 5d orbitals via the magnetic field-induced mixing discussed above. The mechanism appears to be rather general; both Pt centers in MGS are more deshielded, and the effect shows up in all of the principal components of the MS tensor. The question is: What is different between the starting reagents and MGS?

The case is best illustrated by considering an isolated four-coordinate square-planar PtX_4 system, with X being a σ-donating ligand such as a halide or an amine. As previously shown in the literature, a corresponding six-coordinate complex PtX_6 has a much more strongly deshielded Pt center because of additional low-energy unoccupied σ^* orbitals in the direction of σ_{11}. The orbital rotation model explains why the in-plane (σ_{22}, σ_{33}) MS tensor components are more negative: the magnetic field-rotated d_{xz} and d_{yz} orbitals can overlap with the new σ^* orbitals, causing a stronger deshielding induced paramagnetic current density at the Pt center when the additional ligands are present. For a qualitative illustration, see Figure 13, where we

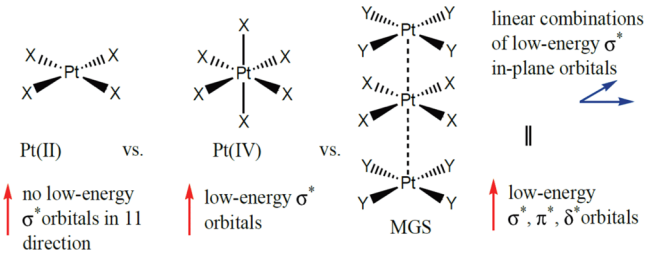

Figure 13. If low-energy unoccupied orbitals can overlap with a 'magnetic field rotated' Pt 5d orbital, a deshielding contribution is obtained in the MS tensor component parallel to the field. This causes deshielding in six-coordinate Pt(IV) vs four-coordinate Pt(II), as shown in ref 82. In MGS, similar orbital interactions are implicated in deshielding contributions from the Pt 5d nonbonding orbitals in all principal MS tensor components relative to the four-coordinate Pt(II) starting reagents.

can see the potential influence of orbital interactions between different Pt centers in MGS. There are two major differences when comparing a Pt center in MGS versus PtX_6: (i) The orbital interactions in the direction of σ_{11} are evidently much weaker in MGS, and (ii) linear combinations of low-energy Pt−Y σ^* orbitals in a neighboring PtY_4 unit give low-energy orbitals of σ^*, π^*, and δ^* symmetry when classified with respect to the Pt−Pt axis. As a consequence, in-plane and out-of-plane 5d orbitals contribute to the deshielding of the Pt center in MGS relative to the starting reagents, affecting all MS tensor components. Moreover, this model explains the sizable deshielding contributions of the Pt $5d_{z^2}$ orbitals in the σ_{22}, σ_{33} tensor components found in the LMO analysis: As Figure S14 shows, the rotated orbital requires interactions of π symmetry in the σ_{11} direction to create effective paramagnetic tensor contributions.

The distance to the neighboring Pt centers evidently has a crucial influence on the platinum MS tensor. MGS, with its comparatively shorter Pt−Pt contacts, affords the orbital interactions described above that result in net deshielding along the direction of σ_{11}. Keeping in mind that at larger distances orbital interactions decrease exponentially, the Pt−Pt distances in the starting materials are likely too large to give significant orbital interactions in the σ_{11} direction. In MPS, the relative spatial orientation of the chloride and ammonium Pt units and the large distances between Pt centers prevents direct metal−metal orbital interaction, hence its MS parameters are closer to those of the starting reagents. While MS tensor calculations of large cluster models for MPS were not successful, a cruder electrostatic model for the MPS environment using ZORA/PBE/TZP Mulliken charges taken from an ADF-BAND calculation indeed results in Pt MS not very far from those of **A** and **B′**: 3821 and 2958 ppm for the $[Pt(NH_3)_4]^{2+}$ and $[PtCl_4]^{2-}$ moiety, respectively. The geometry optimization gave Pt−Cl distances close to the experiment, unlike K_2PtCl_4. Therefore the comparison with **B′** rather than

dx.doi.org/10.1021/ja4076277 | J. Am. Chem. Soc. 2014, 136, 1333−1351

B seems appropriate. However, the results should be interpreted with caution considering that there are many factors which may influence the calculated data (e.g., the quality of the optimized MPS structure, partial charges, and the size of the supercell used in the electrostatic model). Further investigation of this computationally challenging system will be left for a follow-up study.

CONCLUSIONS

Multinuclear SSNMR has been used in conjunction with complementary pXRD and XANES/EXAFS experiments to investigate the structure of Magnus' green and pink salts, $[(Pt(NH_3)_4][PtCl_4]$, as well as their precursors, $Pt(NH_3)_4Cl_2 \cdot H_2O$ and K_2PtCl_4. In order to produce MPS with only a minimum of MGS coproduct, a new synthetic procedure employing acetone and water was implemented. All methods of characterization, including SSNMR and pXRD, indicate our product is composed largely of the pink salt with small amounts of impurities in the form of the green salt and starting reagents. ^{195}Pt static WURST-CPMG, BRAIN-CP/WURST-CPMG, Hahn-echo, and MAS SSNMR experiments show that the ^{195}Pt CS tensor is sensitive to the presence of Pt−Pt metallophilic interactions in these systems and that MPS does not feature such interactions. ^{14}N and ^{35}Cl WURST-CPMG SSNMR experiments illustrate the sensitivity of EFG tensor parameters to small deviations from ideal D_{4h} square-planar symmetry in the $Pt(NH_3)_4Cl_2$ and K_2PtCl_4 compounds, and such experiments also confirm that MPS is composed of square-planar $[Pt(NH_3)_4]^{2+}$ and approximately square-planar $[PtCl_4]^{2-}$ units. EXAFS experiments indicate that the Pt−N and Pt−Cl bond lengths within MPS are similar to those of MGS. A Rietveld refinement of MPS diffraction data resulted in elucidation of several important crystal structure parameters, including the space group, the unit cell parameters, and the atomic positions of Pt, Cl, and N. The crystal structure of MPS features a noncolumnar arrangement of square-planar Pt units; this motif is unique from that of MGS and the reagents and precludes any possibility of metallophilic Pt−Pt interactions within MPS. First principles calculations were performed in order to correlate NMR parameters and molecular structure and confirm that differences in out-of-plane nuclear magnetic shielding give rise to the unique MGS ^{195}Pt SSNMR spectra. The unique structure of MPS, with its absence of Pt−Pt metallophillic interactions, has CS tensors that are similar to starting reagents, consistent with these theoretical models of MS tensor contributions. With conclusive evidence that the ^{195}Pt CS tensor is sensitive to Pt−Pt interactions, we plan to employ this combination of ultrawideline SSNMR along with pXRD techniques to extend our study across a variety of Pt-based systems with Pt−Pt contacts.

ASSOCIATED CONTENT

Supporting Information

Detailed EXAFS and XANES analysis, summary of MPS structure determination, tabulated results of FT-IR, elemental analysis, and ^{1}H MAS SSNMR experiments, additional SSNMR spectra, complete SSNMR experimental parameters, pXRD refinement parameters for MGS, illustrations of calculated Pt magnetic shielding in $Pt(NH_3)_4Cl_2 \cdot H_2O$ and MGS, detailed Pt LMO and NLMO contributions to Pt magnetic shielding. This material is available free of charge via the Internet at http://pubs.acs.org.

AUTHOR INFORMATION

Corresponding Authors

rschurko@uwindsor.ca
jochena@buffalo.edu

Notes

The authors declare no competing financial interest.

ACKNOWLEDGMENTS

B.E.G.L. thanks the Ontario Ministry of Training, Colleges, and Universities for a Queen Elizabeth II Ontario Graduate Scholarship in Science and Technology (QEII-GSST). R.W.S. thanks the Natural Sciences and Engineering Research Council (NSERC, Canada), the Canadian Foundation for Innovation, the Ontario Innovation Trust and the University of Windsor for support. R.W.S. also thanks the Ontario Ministry of Research and Innovation for an Early Researcher Award, and acknowledges the Centre for Catalysis and Materials Research (CCMR) at the University of Windsor for additional funding. Dr. Kris J. Harris and Mr. Stanislav Veinberg are acknowledged for their assistance with BRAIN-CP/WURST-CPMG experiments. Prof. Walter Caseri (Swiss Federal Institute of Technology Zurich) is thanked for very helpful comments regarding the synthesis of MPS. Access to the 900 MHz NMR spectrometer was provided by the National Ultrahigh-Field NMR Facility for Solids (Ottawa, Canada), a national research facility funded by the Canada Foundation for Innovation, the Ontario Innovation Trust, Recherche Québec, the National Research Council Canada, and Bruker BioSpin and managed by the University of Ottawa (www.nmr900.ca). The Natural Sciences and Engineering Research Council of Canada (NSERC) is acknowledged for a Major Resources Support grant. We are grateful to Dr. Victor Terskikh and Dr. Eric Ye for experiments run at the National Ultrahigh-field NMR Facility. The Brookhaven National Laboratory Chemistry Department and National Synchrotron Light Source are funded by the U.S. Department of Energy, Office of Science, Office of Basic Energy Sciences, under contract AC02-98CH10886. This work has been supported by grants CHE 0952253 and 1265833 from the National Science Foundation. M.S. is grateful for financial support from the Ministry of Science and Higher Education in Poland ("Mobility Plus" program) and from the Foundation for Polish Science ("START" scholarship). The authors would like to acknowledge the Center for Computational Research (CCR) at the University at Buffalo for providing computational resources. M.S. thanks Dr. James Hooper for some technical advice.

REFERENCES

(1) Williams, J. A. G. In *Photochemistry and Photophysics of Coordination Compounds II*; Balzani, V., Campagna, S., Eds.; Springer DE: Berlin, 2007; Vol. *281*, pp 205−268.
(2) Qin, Z. Q.; Jennings, M. C.; Puddephatt, R. J. *Inorg. Chem.* **2003**, *42*, 1956−1965.
(3) Mdleleni, M. M.; Bridgewater, J. S.; Watts, R. J.; Ford, P. C. *Inorg. Chem.* **1995**, *34*, 2334−2342.
(4) Hissler, M.; Connick, W. B.; Geiger, D. K.; McGarrah, J. E.; Lipa, D.; Lachicotte, R. J.; Eisenberg, R. *Inorg. Chem.* **2000**, *39*, 447−457.
(5) Connick, W. B.; Henling, L. M.; Marsh, R. E.; Gray, H. B. *Inorg. Chem.* **1996**, *35*, 6261−6265.
(6) Brooks, J.; Babayan, Y.; Lamansky, S.; Djurovich, P. I.; Tsyba, I.; Bau, R.; Thompson, M. E. *Inorg. Chem.* **2002**, *41*, 3055−3066.
(7) Jain, V. K.; Jain, L. *Coord. Chem. Rev.* **2010**, *254*, 2848−2903.
(8) Eryazici, I.; Moorefield, C. N.; Newkome, G. R. *Chem. Rev.* **2008**, *108*, 1834−1895.
(9) Reedijk, J. *Chem. Commun.* **1996**, 801−806.

(10) Sundquist, W. I.; Lippard, S. J. *Coord. Chem. Rev.* **1990**, *100*, 293−322.
(11) Knipp, M. *Curr. Med. Chem.* **2009**, *16*, 522−537.
(12) Momekov, G.; Momekova, D. *Expert Opin. Ther. Pat.* **2006**, *16*, 1383−1403.
(13) Todd, R. C.; Lippard, S. J. *Metallomics* **2009**, *1*, 280−291.
(14) Lecointe, P.; Macquet, J. P.; Butour, J. L.; Paoletti, C. *Mutat. Res.* **1977**, *48*, 139−143.
(15) Lippert, B. *Prog. Inorg. Chem.* **1989**, *37*, 1−97.
(16) Vanbeusichem, M.; Farrell, N. *Inorg. Chem.* **1992**, *31*, 634−639.
(17) Doerrer, L. H. *Dalton Trans.* **2010**, *39*, 3543−3553.
(18) Caseri, W. *Platinum Met. Rev.* **2004**, *48*, 91−100.
(19) Roundhill, D. M.; Gray, H. B.; Che, C. M. *Acc. Chem. Res.* **1989**, *22*, 55−61.
(20) Miller, J. S. *Inorg. Chem.* **1976**, *15*, 2357−2360.
(21) Miller, J. S.; Epstein, A. J. *Prog. Inorg. Chem.* **1976**, *20*, 1.
(22) Pyykko, P. *Chem. Rev.* **1997**, *97*, 597−636.
(23) Pyykko, P. *Angew. Chem., Int. Ed.* **2004**, *43*, 4412−4456.
(24) Jiang, Y.; Alvarez, S.; Hoffmann, R. *Inorg. Chem.* **1985**, *24*, 749−757.
(25) Scherbaum, F.; Grohmann, A.; Huber, B.; Kruger, C.; Schmidbaur, H. *Angew. Chem., Int. Ed.* **1988**, *27*, 1544−1546.
(26) Magnus, G. *Pogg. Ann.* **1828**, *11*, 242.
(27) Atoji, M.; Richardson, J. W.; Rundle, R. E. *J. Am. Chem. Soc.* **1957**, *79*, 3017−3020.
(28) Interrante, L.; Messmer, R. P. *Inorg. Chem.* **1971**, *10*, 1174−1180.
(29) Musselman, R. L. *Inorg. Chim. Acta* **2008**, *361*, 820−830.
(30) Bremi, J.; Brovelli, D.; Caseri, W.; Hahner, G.; Smith, P.; Tervoort, T. *Chem. Mater.* **1999**, *11*, 977−994.
(31) Bremi, J.; Gramlich, V.; Caseri, W.; Smith, P. *Inorg. Chim. Acta* **2001**, *322*, 23−31.
(32) Hertel, E.; Schneider, K. *Z. Anorg. Allg. Chem.* **1931**, *202*, 77−80.
(33) Jorgensen, S. M.; Sorensen, S. P. L. *Z. Anorg. Allg. Chem.* **1906**, *48*, 441.
(34) Still, B. M.; Kumar, P. G. A.; Aldrich-Wright, J. R.; Price, W. S. *Chem. Soc. Rev.* **2007**, *36*, 665−686.
(35) Priqueler, J. R. L.; Butler, I. S.; Rochon, F. D. *Appl. Spectrosc. Rev.* **2006**, *41*, 185−226.
(36) Truflandier, L. A.; Autschbach, J. *J. Am. Chem. Soc.* **2010**, *132*, 3472−3483.
(37) Truflandier, L. A.; Sutter, K.; Autschbach, J. *Inorg. Chem.* **2011**, *50*, 1723−1732.
(38) Sutter, K.; Truflandier, L. A.; Autschbach, J. *ChemPhysChem* **2011**, *12*, 1448−1455.
(39) Pregosin, P. S. In *Annual Reports on NMR Spectroscopy*; Webb, G. A., Ed.; Academic Press: New York, 1986; Vol. *17*, p 356.
(40) Goodfellow, R. J. In *Multinuclear NMR*; 1st ed.; Mason, J., Ed.; Plenum Press: New York, 1987, p 639.
(41) Lucier, B. E. G.; Reidel, A. R.; Schurko, R. W. *Can. J. Chem.* **2011**, *89*, 919−937.
(42) O'Dell, L. A.; Schurko, R. W. *Chem. Phys. Lett.* **2008**, *464*, 97−102.
(43) Tang, J. A.; O'Dell, L. A.; Aguiar, P. M.; Lucier, B. E. G.; Sakellariou, D.; Schurko, R. W. *Chem. Phys. Lett.* **2008**, *466*, 227−234.
(44) O'Dell, L. A.; Rossini, A. J.; Schurko, R. W. *Chem. Phys. Lett.* **2009**, *468*, 330−335.
(45) Kupce, E.; Freeman, R. *J. Magn. Reson., Ser. A* **1995**, *115*, 273−276.
(46) Bhattacharyya, R.; Frydman, L. *J. Chem. Phys.* **2007**, *127*, 194503(1)−194503(8).
(47) Larsen, F. H.; Jakobsen, H. J.; Ellis, P. D.; Nielsen, N. C. *J. Phys. Chem. A* **1997**, *101*, 8597−8606.
(48) Harris, K. J.; Lupulescu, A.; Lucier, B. E. G.; Frydman, L.; Schurko, R. W. *J. Magn. Reson.* **2012**, *224*, 38−47.
(49) Hudson, Z. M.; Sun, C.; Harris, K. J.; Lucier, B. E. G.; Schurko, R. W.; Wang, S. N. *Inorg. Chem.* **2011**, *50*, 3447−3457.
(50) MacGregor, A. W.; O'Dell, L. A.; Schurko, R. W. *J. Magn. Reson.* **2011**, *208*, 103−113.
(51) Pallier, C.; Leyssale, J. M.; Truflandier, L. A.; Bui, A. T.; Weisbecker, P.; Gervais, C.; Fischer, H. E.; Sirotti, F.; Teyssandier, F.; Chollon, G. *Chem. Mater.* **2013**, *25*, 2618−2629.
(52) Dudenko, D. V.; Williams, P. A.; Hughes, C. E.; Antzutkin, O. N.; Velaga, S. P.; Brown, S. P.; Harris, K. D. M. *J. Phys. Chem. C* **2013**, *117*, 12258−12265.
(53) Brouwer, D. H.; Cadars, S.; Eckert, J.; Liu, Z.; Terasaki, O.; Chmelka, B. F. *J. Am. Chem. Soc.* **2013**, *135*, 5641−5655.
(54) Brouwer, D. H. *J. Magn. Reson.* **2008**, *194*, 136−146.
(55) Mafra, L.; Rocha, J.; Fernandez, C.; Castro, G. R.; Garcia-Granda, S.; Espina, A.; Khainakov, S. A.; Garcia, J. R. *Chem. Mater.* **2008**, *20*, 3944−3953.
(56) Alam, T. M.; Clawson, J. S.; Bonhomme, F.; Thoma, S. G.; Rodriguez, M. A.; Zheng, S.; Autschbach, J. *Chem. Mater.* **2008**, *20*, 2205−2217.
(57) Martineau, C.; Fayon, F.; Legein, C.; Buzare, J. Y.; Body, M.; Massiot, D.; Goutenoire, F. *Dalton Trans.* **2008**, 6150−6158.
(58) Ashbrook, S. E.; Cutajar, M.; Pickard, C. J.; Walton, R. I.; Wimperis, S. *Phys. Chem. Chem. Phys.* **2008**, *10*, 5754−5764.
(59) Widdifield, C. M.; Tang, J. A.; Macdonald, C. L. B.; Schurko, R. W. *Magn. Reson. Chem.* **2007**, *45*, S116−S128.
(60) Harris, R. K.; Ghi, P. Y.; Hammond, R. B.; Ma, C. Y.; Roberts, K. J.; Yates, J. R.; Pickard, C. J. *Magn. Reson. Chem.* **2006**, *44*, 325−333.
(61) Body, M.; Silly, G.; Legein, C.; Buzare, J. Y.; Calvayrac, F.; Blaha, P. *J. Solid State Chem.* **2005**, *178*, 3655−3661.
(62) Fyfe, C. A.; Brouwer, D. H.; Lewis, A. R.; Villaescusa, L. A.; Morris, R. E. *J. Am. Chem. Soc.* **2002**, *124*, 7770−7778.
(63) Johnston, K. E.; O'Keefe, C. A.; Gauvin, R. M.; Trébosc, J.; Delevoye, L.; Amoureux, J.-P.; Popoff, N.; Taoufik, M.; Oudatchin, K.; Schurko, R. W. *Chem.—Eur. J.* **2013**, *19*, 12396−12414.
(64) Hamaed, H.; Pawlowski, J. M.; Cooper, B. F. T.; Fu, R. Q.; Eichhorn, S. H.; Schurko, R. W. *J. Am. Chem. Soc.* **2008**, *130*, 11056−11065.
(65) Honda, K.; Chiba, K.; Tsuchida, E.; Frank, A. J. *J. Mater. Sci.* **1989**, *24*, 4004−4008.
(66) Palkin, V. A.; Kuzina, T. A.; Kuzmina, N. N.; Shchelokov, R. N. *J. Anal. Chem. USSR* **1980**, *25*, 1291−1295.
(67) Yamada, S. *J. Am. Chem. Soc.* **1951**, *73*, 1579−1580.
(68) Massiot, D.; Farnan, I.; Gautier, N.; Trumeau, D.; Florian, P.; Grandinetti, P. J. *J. Chim. Phys. Phys.-Chim. Biol.* **1995**, *92*, 1847−1850.
(69) Medek, A.; Frydman, V.; Frydman, L. *J. Phys. Chem. A* **1999**, *103*, 4830−4835.
(70) Tang, J. A.; Masuda, J. D.; Boyle, T. J.; Schurko, R. W. *ChemPhysChem* **2006**, *7*, 117−130.
(71) Lipton, A. S.; Wright, T. A.; Bowman, M. K.; Reger, D. L.; Ellis, P. D. *J. Am. Chem. Soc.* **2002**, *124*, 5850−5860.
(72) O'Dell, L. A.; Ratcliffe, C. I. *Chem. Commun.* **2010**, *46*, 6774−6776.
(73) Eichele, K. *WSolids1*, version 1.20.15; Universität of Tübingen: Tübingen, Germany, 2011.
(74) Massiot, D.; Fayon, F.; Capron, M.; King, I.; Le Calve, S.; Alonso, B.; Durand, J.-O.; Bujoli, B.; Gan, Z.; Hoatson, G. *Magn. Reson. Chem.* **2002**, *40*, 70−76.
(75) *ADF2011.01* and *ADF2012.01*, Vrije Universiteit: Amsterdam, The Netherlands, http://www.scm.com/ADF/; accessed December 9, 2013.
(76) Velde, G. T.; Bickelhaupt, F. M.; Baerends, E. J.; Guerra, C. F.; Van Gisbergen, S. J. A.; Snijders, J. G.; Ziegler, T. *J. Comput. Chem.* **2001**, *22*, 931−967.
(77) Perdew, J. P.; Burke, K.; Ernzerhof, M. *Phys. Rev. Lett.* **1996**, *77*, 3865−3868.
(78) Perdew, J. P.; Burke, K.; Ernzerhof, M. *Phys. Rev. Lett.* **1997**, *78*, 1396−1396.
(79) Ernzerhof, M.; Scuseria, G. E. *J. Chem. Phys.* **1999**, *110*, 5029−5036.
(80) Adamo, C.; Barone, V. *J. Chem. Phys.* **1999**, *110*, 6158−6170.
(81) Sterzel, M.; Autschbach, J. *Inorg. Chem.* **2006**, *45*, 3316−3324.

(82) Autschbach, J.; Zheng, S. H. *Magn. Reson. Chem.* **2008**, *46*, S45−S55.
(83) Davis, J. C.; Buhl, M.; Koch, K. R. *J. Chem. Theory Comput.* **2012**, *8*, 1344−1350.
(84) van Lenthe, E.; Baerends, E. J.; Snijders, J. G. *J. Chem. Phys.* **1993**, *99*, 4597−4610.
(85) Wolff, S. K.; Ziegler, T.; van Lenthe, E.; Baerends, E. J. *J. Chem. Phys.* **1999**, *110*, 7689−7698.
(86) Autschbach, J.; Zurek, E. *J. Phys. Chem. A* **2003**, *107*, 4967−4972.
(87) Glendening, E. D.; Badenhoop, J. K.; Reed, A. E.; Carpenter, J. E.; Bohmann, J. A.; Morales, C. M.; Weinhold, F. *NBO 5.0*; Theoretical Chemistry Institute, University of Wisconsin: Madison, WI, 2001.
(88) Weinhold, F. In *Encyclopedia of Computational Chemistry*; von Ragué Schleyer, P., Ed.; John Wiley & Sons: Chichester, 1998, pp 1792−1811.
(89) Autschbach, J. *J. Chem. Phys.* **2008**, *128*, 164111−12.
(90) Cox, E. G. *J. Chem. Soc.* **1932**, 1912−1920.
(91) Mais, R. H. B.; Wood, A. M.; Owston, P. G. *Acta Crystallogr. B* **1972**, *B28*, 393−399.
(92) Baroni, S.; de Gironcoli, S.; Dal Corso, A.; Giannozzi, P. *Pwscf, Plane-Wave Self-Consistent Field*; SISSA and DEMOCRITOS National Simulation Center: Trieste, Italy, 2009.
(93) Giannozzi, P.; Baroni, S.; Bonini, N.; Calandra, M.; Car, R.; Cavazzoni, C.; Ceresoli, D.; Chiarotti, G. L.; Cococcioni, M.; Dabo, I.; Dal Corso, A.; de Gironcoli, S.; Fabris, S.; Fratesi, G.; Gebauer, R.; Gerstmann, U.; Gougoussis, C.; Kokalj, A.; Lazzeri, M.; Martin-Samos, L.; Marzari, N.; Mauri, F.; Mazzarello, R.; Paolini, S.; Pasquarello, A.; Paulatto, L.; Sbraccia, C.; Scandolo, S.; Sclauzero, G.; Seitsonen, A. P.; Smogunov, A.; Umari, P.; Wentzcovitch, R. M. *J. Phys.: Condens. Matter* **2009**, *21*, 395502/1−395502/19.
(94) Vanderbilt, D. *Phys. Rev. B* **1990**, *41*, 7892−7895.
(95) Morosin, B.; Fallon, P.; Valentine, J. S. *Acta Crystallogr. B* **1975**, *31*, 2220−2223.
(96) Cohen, A. J.; Mori-Sanchez, P.; Yang, W. T. *Science* **2008**, *321*, 792−794.
(97) Moore, B.; Autschbach, J. *ChemistryOpen* **2012**, *1*, 184−194.
(98) Hammersley, A. P.; Svensson, S. O.; Hanfland, M.; Fitch, A. N.; Hausermann, D. *High Pressure Res.* **1996**, *14*, 235−248.
(99) Rietveld, H. *J. Appl. Crystallogr.* **1969**, *2*, 65−71.
(100) Larson, A. C.; Von Dreele, R. B. General Structure Analysis System (GSAS). *Report LA-UR-86-748*; Los Alamos National Laboratory: Los Alamos, NM, 2004.
(101) Toby, B. H. *J. Appl. Crystallogr.* **2001**, *34*, 210−213.
(102) Tang, J. A.; Kogut, E.; Norton, D.; Lough, A. J.; McGarvey, B. R.; Fekl, U.; Schurko, R. W. *J. Phys. Chem. B* **2009**, *113*, 3298−3313.
(103) Sparks, S. W.; Ellis, P. D. *J. Am. Chem. Soc.* **1986**, *108*, 3215−3218.
(104) Keller, H. J.; Rupp, H. H. *Z. Naturforsch., A: Phys. Sci.* **1970**, *A 25*, 312−313.
(105) Keller, H. J.; Rupp, H. H. *Z. Naturforsch., A: Phys. Sci.* **1971**, *A 26*, 785−786.
(106) Briand, G. G.; Smith, A. D.; Schatte, G.; Rossini, A. J.; Schurko, R. W. *Inorg. Chem.* **2007**, *46*, 8625−8637.
(107) O'Dell, L. A.; Schurko, R. W.; Harris, K. J.; Autschbach, J.; Ratcliffe, C. I. *J. Am. Chem. Soc.* **2011**, *133*, 527−546.
(108) O'Dell, L. A. *Prog. Nucl. Magn. Reson. Spectrosc.* **2011**, *59*, 295−318.
(109) Harris, K. J.; Veinberg, S. L.; Mireault, C. R.; Lupulescu, A.; Frydman, L.; Schurko, R. W. *Chem.—Eur. J.* **2013**, *19*, 16469−16475.
(110) O'Dell, L. A.; Schurko, R. W. *J. Am. Chem. Soc.* **2009**, *131*, 6658−6659.
(111) O'Dell, L. A.; Schurko, R. W. *Phys. Chem. Chem. Phys.* **2009**, *11*, 7069−7077.
(112) Penner, G. H.; Webber, R.; O'Dell, L. A. *Can. J. Chem.* **2011**, *89*, 1036−1046.
(113) O'Dell, L. A.; Ratcliffe, C. I.; Kong, X. Q.; Wu, G. *J. Phys. Chem. A* **2012**, *116*, 1008−1014.
(114) Bryce, D. L.; Sward, G. D.; Adiga, S. *J. Am. Chem. Soc.* **2006**, *128*, 2121−2134.
(115) Chapman, R. P.; Bryce, D. L. *Phys. Chem. Chem. Phys.* **2007**, *9*, 6219−6230.
(116) Bryce, D. L.; Bultz, E. B. *Chem.—Eur. J.* **2007**, *13*, 4786−4796.
(117) Gordon, P. G.; Brouwer, D. H.; Ripmeester, J. A. *J. Phys. Chem. A* **2008**, *112*, 12527−12529.
(118) Gordon, P. G.; Brouwer, D. H.; Ripmeester, J. A. *ChemPhysChem* **2010**, *11*, 260−268.
(119) Chapman, R. P.; Widdifield, C. M.; Bryce, D. L. *Prog. Nucl. Magn. Reson. Spectrosc.* **2009**, *55*, 215−237.
(120) Chapman, R. P.; Bryce, D. L. *Phys. Chem. Chem. Phys.* **2009**, *11*, 6987−6998.
(121) Rossini, A. J.; Mills, R. W.; Briscoe, G. A.; Norton, E. L.; Geier, S. J.; Hung, I.; Zheng, S.; Autschbach, J.; Schurko, R. W. *J. Am. Chem. Soc.* **2009**, *131*, 3317−3330.
(122) Hung, I.; Shetty, K.; Ellis, P. D.; Brey, W. W.; Gan, Z. H. *Solid State Nucl. Magn. Reson.* **2009**, *36*, 159−163.
(123) Perras, F. A.; Bryce, D. L. *J. Magn. Reson.* **2011**, *213*, 82−89.
(124) Zurek, E.; Pickard, C. J.; Autschbach, J. *J. Phys. Chem. A* **2009**, *113*, 4117−4124.
(125) Hansen, A. E.; Bouman, T. D. *J. Chem. Phys.* **1989**, *91*, 3552−3560.
(126) Widdifield, C. M.; Schurko, R. W. *Concept. Magnetic Res. A* **2009**, *34A*, 91−123.